An update to this article is included at the end

Journal of Petroleum Science and Engineering 216 (2022) 110754

Contents lists available at ScienceDirect

Journal of Petroleum Science and Engineering

journal homepage: www.elsevier.com/locate/petrol

# Lattice Boltzmann study of dissolution in porous media: Comparison of VOP with VOF-curved boundary coupling

Elham Kashani [a], Ali Mohebbi [a], Amir Ehsan Feili Monfared [b,*], Amir Raoof [c]

[a] Department of Chemical Engineering, Faculty of Engineering, Shahid Bahonar University of Kerman, Kerman, Iran
[b] Department of Chemical Engineering, Graduate University of Advanced Technology, Kerman, Iran
[c] Environmental Hydrogeology, Department of Earth Sciences, Utrecht University, Utrecht, the Netherlands

ARTICLE INFO

*Keywords:*
Lattice Boltzmann method
Volume of fluid method
Volume of pixel
Heterogeneous dissolution
Porous media
Curved boundary condition

ABSTRACT

In dissolution processes, during geometry evolution, the two-phase interface is continuously changed. For tracking the position of the interface, the method of combining VOF with curved boundary schemes was presented in this research. Since the combination would be rather complex, in addition to the original approach, a simplified approximate approach was also introduced. Further, for simulating heterogeneous dissolution in lattice Boltzmann (LB) framework, the volume of pixel (VOP) method has been widely used by researchers. Since the area of the solid-fluid interface is not captured by this method, the study of its validity was also presented in this research. For this purpose, simulations of calcium carbonate dissolution by hydrochloric acid in simple and complex porous media were performed. In addition to the VOP method, the volume of fluid (VOF) method in which the solid-fluid interface is tracked, was also applied for all cases of simulations. The results revealed that from a dissolution perspective, the performance of the VOF-curved boundary combination is essentially similar to that of the VOF-bounce back combination. However, the algorithm of bounce back was found to be more than 10% computationally efficient. Also, comparison of the outcomes from VOP and VOF indicated that VOP intrinsically overestimates the surface area of reactions by about 25–35%, which fictitiously leads to 20–30% higher reaction rates and nearly 20–30% less dissolution times. Hence, it was deduced that the temporal outcomes of VOP may not be valid. However, from a non-temporal perspective, the dissolution patterns of both methods were found to be essentially similar.

## 1. Introduction

Numerical simulation of heterogeneous dissolution/precipitation processes is widely used in many (geo-)chemical applications such as mining (Fredd and Fogler, 1998), underground water engineering (Griebler et al., 2016), geothermal energy (Hoop et al., 2021), and hydrocarbon recovery processes (Duquerroix et al., 1990; Han et al., 2020). Addressing the associated numerical simulation challenges and possible improvements have been the subject of several studies (Fogler and Hoefner, 1988; Menke et al., 2015; Quintard and Whitaker, 1994). Two challenges of simulating heterogeneous reactions include tracking the interface and calculating the instantaneous specific surface area of the solid-fluid interface (Přikryl et al., 2017). The evolution of interface is tracked by several methods such as phase-field (PF) (Tong et al., 2001), cellular automaton (CA) (Shin and Hong, 2002), level set (LS) (Dugast et al., 2020; Tan and Zabaras, 2006, 2007), and volume of fluid (VOF) (Rudman, 1997). Despite the reputation of these methods, they suffer from several inherent limitations (Scardovelli and Zaleski, 1999). For example, in the case of complex geometries such as those of porous media, their employment would add complexity to the algorithms and can considerably increase the computational costs (Chen et al., 2013; Scardovelli and Zaleski, 1999). Due to these limitations, in simulations of free-surface and interfacial flows, consideration of more than a few droplets or bubbles would be a challenging task (Scardovelli and Zaleski, 1999). In the lattice Boltzmann method, the employment of such surface tracking techniques has not been popular so far, and, alternatively, the simple method of volume of pixel (VOP) (Chen et al., 2013) has been widely employed (Chen et al., 2013; Liu et al., 2018; Mostaghimi et al., 2016; Yoon et al., 2015). For example, in 2007, Kang et al. proposed an improved lattice Boltzmann model for multicomponent reactive

* Corresponding author.
*E-mail addresses:* amohebbi@uk.ac.ir, amohebbi2002@yahoo.com (A. Mohebbi), Ehsan.monfared@outlook.com, e.monfared@kgut.ac.ir (A.E. Feili Monfared), a.raoof@uu.nl (A. Raoof).

https://doi.org/10.1016/j.petrol.2022.110754
Received 11 February 2022; Received in revised form 4 June 2022; Accepted 8 June 2022
Available online 14 June 2022
0920-4105/© 2022 Elsevier B.V. All rights reserved.

transport and utilized the volume of pixel method to calculate volumetric dissolution rates. They found that by applying the new boundary condition, the solute mass is strictly conserved by heterogeneous reactions that were not observed while using the thermal boundary condition (Kang et al., 2007). Chen et al. (2014) adopted VOP to track the fluid-solid interface for simulating diffusion-reaction processes involving dissolution and precipitation. Their results revealed that precipitation would have opposite effects on the underlying dissolution process such that precipitates cover the surface solid-phase; thus, the reactive surface is separated from the reactive components (Chen et al., 2014). In 2018, a thermochemical ablation model of carbon/carbon composite based on the lattice Boltzmann method was established by Wang and Zhu (2018). In this study, flow, diffusion, chemical reaction, and heat transfer were simulated by lattice Boltzmann method (LBM) and the VOP was used for the evolution of the solid phase (Wang and Zhu, 2018). Carbonate rock dissolution process was studied by Zhou et al. (2020), where the flow of two immiscible fluids, solute transport, and heat transfer were simulated using the Shan-Chen multiphase multicomponent, mass transport, and multicomponent thermal lattice Boltzmann models, respectively. In their study, the state of the solid phase was updated by the volume of pixel method (Zhou et al., 2020). In more recent work, Taahodi et al. (2021) investigated porosity-permeability variations under different regimes of non-isothermal dissolution in porous media and used VOP to track the evolution of the solid phase. In their study, by performing several simulations, the dependency of dominant dissolution patterns on dimensionless numbers were discussed, which could be wormhole, uniform, or face dissolution patterns (Taahodi et al., 2021). Zhang et al. (2022) applied LBM to dual-porosity domains to investigate the effect of heterogeneity on mineral dissolution and permeability evolution in porous media. They adopted the VOP approach for calculating the instantaneous solid volumes during chemical reactions. In their study, four types of porosity-permeability relationship were observed. In addition, they found that the dissolution patterns depend on the pore heterogeneity at high Peclet and Damkohler numbers (Zhang et al., 2022).

When using the VOP method, the orientation and the area of the fluid-solid interfaces are not captured and a fixed value of unity is assigned to specific surface area of all interface nodes. Although this approach provides simplicity and efficiency to the lattice Boltzmann method in dealing with complex geometries, the assumption of invariant surface area is questionable and its variations can directly affect local reaction rates of solid-phase volume changes (Yoon et al., 2015). Thus, in this study, we explore the performance of VOP and its comparison with surface capturing methods. As the computational costs of surface capturing techniques in complex geometries are high (Chen et al., 2013; Scardovelli and Zaleski, 1999), special attention was paid to porous media and simulation performances with and without capturing surface in terms of both accuracy and the efficiency of the methods. We have adopted VOF as the surface tracking technique and provided ways for its efficient implementation in LBM. We should note that, although not common, VOF has been coupled with LBM methods. For example, Molins et al. (2020) presented a benchmark problem for the dissolution process at the pore scale. For this purpose, they employed five different solvers including OpenFOAM-DBS, Vortex, Chombo-Crunch, dissolFoam, and a lattice Boltzmann program. In their LBM algorithm, VOF was used to capture the area of the fluid-solid interface during the dissolution progress. The results of the five codes showed remarkable agreement both quantitatively and qualitatively in terms of surface area and shape evolution (Molins et al., 2020). In another work, Ju et al. (2020) employed VOF to explore the application of a boundary scheme for convection-diffusion problems in domains with irregular pore structures. Their results were in agreement with analytical solutions where a second-order accuracy for a straight wall was found (Ju et al., 2020).

LBM is widely used for diverse pore-scale simulations (Guo and Zhao, 2002; Pan et al., 2006) due to the possibility of employing parallel algorithms as well as the simplicity and efficiency of the bounce-back boundary condition to be used in complex porous media (Bouzidi et al., 2001; Yin and Zhang, 2012). However, the bounce-back boundary condition, in contrast to curved boundary methods (Izam et al., 2011), cannot accurately reconstruct the smooth solid boundaries and replaces the interface with intersecting steps. Some studies (Kao and Yang, 2008; Mei et al., 2002; Xu et al., 2016; Yu et al., 2003) have explored the undesirable effects of this approximation on momentum transport. However, its impacts on mass transport properties and medium dissolution patterns have not been explored so far, which is the focus of this study. We have adopted Chun and Ladd's curved boundary method (Chun and Ladd, 2007) to perform reactive flow simulations with both bounce-back boundary conditions and smooth boundary methods and compared the results of these two approaches. Further, as a smooth reconstruction of curvatures would be preferred in many dissolution problems in engineering applications, the coupling of VOF and curved boundary method is also presented and its performance is compared with that of the conventional bounce back scheme.

## 2. Methodology

### 2.1. Lattice Boltzmann method

Convection-diffusion equation (CDE) describes passive scalars transport such as temperature in heat transfer or concentration in mass problems is defined as (Li et al., 2008):

$$\frac{\partial C}{\partial t} + \nabla \cdot (uC) = \nabla \cdot (D \nabla C) \tag{1}$$

where, t is time (s), D is the diffusion coefficient ($m^2/s$), C is the concentration of a solute ($mol/m^3$) and **u** is velocity vector (m/s), which depends on space and time. LBM is a class of computational fluid dynamic methods for simulation of transport processes such as mass transport. In LBM, a distribution function $g(x,c,t)$in the discrete velocity space, *c*, is defined to recover the CDE. The evolution of this distribution function with the LBGK model of lattice Boltzmann equation can be generally expressed as (Kang et al., 2014):

$$g_i(x + c_i \Delta t, t + \Delta t) - g_i(x,t) = \frac{1}{\tau_c}\left[g_i^{eq}(C,u) - g_i(x,t)\right] \tag{2}$$

where $g_i(x,t) \equiv g(x, c_i, t)$,$\tau_c$is the relaxation time which relates to the diffusion coefficient by $D = (\tau_c - 0.5)RT$, C is concentration, $\mathbf{c}_i$ is the *i*th discrete velocity vector specified as unity (i.e.$C_i \equiv \Delta X/\Delta t = 1$)., $\Delta t$ is the time step and $g_i^{eq}$is the equilibrium distribution function. In this study, the equilibrium model of Ref. (Prasianakis et al., 2017) was employed to enhance Galilean invariance.

$$g_i^{eq}(C,u) = C \prod_{\alpha=x,y} \frac{(1 - 2c_{i\alpha}^2)}{2^{c_{i\alpha}^2}} \left(c_{i\alpha}^2 - 1 + c_{i\alpha}u_\alpha + T_0\right) \tag{3}$$

For the isothermal flow, the temperature is fixed at a constant value $T_0 = RT = c_s^2$where *R* is the gas constant, and $c_s$ is the speed of sound ($c_s = 1/\sqrt{3}$). In addition,uis the velocity vector of fluid flow, which can be calculated from the following lattice Boltzmann equation (LBE) (Kang et al., 2014):

$$f_i(x + c_i \Delta t, t + \Delta t) - f_i(x,t) = \frac{1}{\tau}\left[f_i^{eq}(\rho,u) - f_i(x,t)\right] \tag{4}$$

where $f_i$ is the particle moving distribution function with velocity$c_i$,$\tau$ is the relaxation parameter that is related to the kinematic viscosity by $\nu = (\tau - 0.5)RT$, and $f_i^{eq}$ is the equilibrium distribution function that has the following form in the D2Q9 model (Prasianakis et al., 2017).

$$f_i^{eq}(\rho,u) = \rho \prod_{\alpha=x,y} \frac{(2c_{i\alpha}^2 - 1)}{2^{c_{i\alpha}^2}} \left(c_{i\alpha}^2 - 1 + c_{i\alpha}u_\alpha + u_\alpha^2 + T_0\right) \tag{5}$$

where $\rho$is the density of fluid and function $f_i$ is such that conserves quantities $\rho$and $\vec{J}$(similar to $g_i$, which conserves concentration C) (Kang et al., 2014).

$$\rho = \sum_{i=0}^{8} f_i \tag{6}$$

$$J_\alpha = \rho u_\alpha = \sum_{i=0}^{8} c_{i\alpha} f_i \quad \alpha = x, y \tag{7}$$

$$C = \sum_{i=0}^{8} g_i \tag{8}$$

For the nine-speed LBM model employed in this study, discrete velocities are defined as (Kang et al., 2014)

$$c_i = \begin{cases} 0,0 \quad (i=0) \\ \left(\cos\frac{(i-1)\pi}{2}, \sin\frac{(i-1)\pi}{2}\right) \quad (i=1-4) \\ \sqrt{2}\left(\cos\left[\frac{(i-5)\pi}{2}+\frac{\pi}{4}\right], \sin\left[\frac{(i-5)\pi}{2}+\frac{\pi}{4}\right]\right) \quad (i=5-8) \end{cases} \tag{9}$$

Several previous studies (d'Humières and Ginzburg, 2009; Ginzburg, 2005a; Pan et al., 2006) have shown that the common BGK collision operator suffers from viscosity-dependent permeability. For preventing this problem and also improving the numerical stability, a double multi-relaxation time (MRT) scheme (Cui et al., 2016; Lallemand and Luo, 2000) is adopted in this study.

### 2.1.1. Reaction boundary condition

For linear heterogeneous reactions at the macroscopic level, the boundary condition is mathematically formulated as (Ju et al., 2020):

$$D\frac{\partial C_b}{\partial n} = k_r(C_b - C_{eq}) \tag{10}$$

where $C_b$ and $C_{eq}$ are the solute concentration at the boundary lattice nodes and equilibrium concentration, respectively, $k_r$ is the constant rate of chemical reaction (m/s) and **n** is the outward surface normal into the fluid domain (m). Eq. (10) describes the balance between the mineral dissolution rate and the normal flux due to diffusion into the surface. In this research, this condition in LBM framework was implemented by applying the boundary condition presented by Ju et al. (2020). According to Ju et al. (2020), the nodes are generally classified into three categories of fluid, solid and boundary nodes. For a better explanation of the employed boundary method, an arbitrary curved boundary is shown in Fig. 1.

Generally, three types of lattice nodes are defined: nodes that are fully occupied by fluid (called fluid nodes), those fully occupied by solid and have no neighboring fluid node (called solid nodes), and, finally, those that are either partially solid or have at least one fluid node in their neighborhood (called boundary nodes). Having determined the node types, solute concentrations at boundary nodes ($C_b$) are calculated as (Ju et al., 2020):

$$C_b = \frac{2\sum_{i\in A_s} n.c_i g_{i'} - \sum_{i\in A_{ff}} n.c_i g_i}{2\sum_{i\in A_s} n.c_i \omega_i + \gamma k_r} \tag{11}$$

where $\gamma = \tau_c/(\tau_c - 0.5)$, $i'$is the reverse direction of i, $A_s$ include the links that come from solid nodes (i.e., unknown links) and the rest of the links are included in $A_{ff}$ (which come from the fluid or boundary nodes and they are towards a fluid or other boundary nodes). From dot product definition, $n.c_i = |n||c_i|\cos\alpha$,$\alpha$ is the angle between the normal vector of the interface and velocity link, which is obtained by VOF method presented in Section 2.2. After calculating $C_b$, the bounce-back rule of the nonequilibrium distribution function, proposed by He et al. (1998), is employed to determine the unknown distribution functions. For example, for the boundary node A in Fig. 1 we can write:

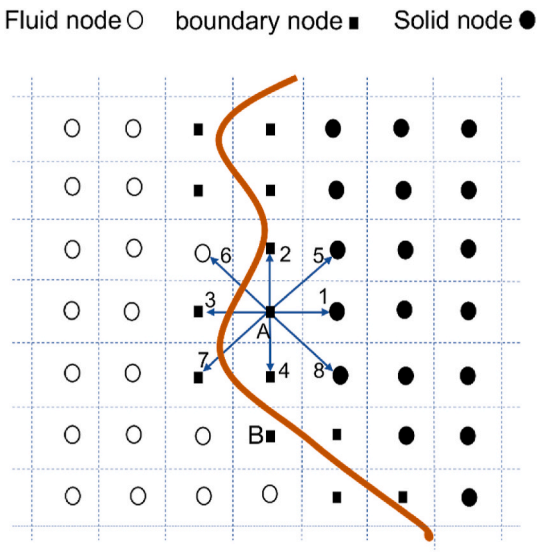


**Fig. 1.** Schematic of a curved boundary and definition of different types of nodes (dashed squares show the boundary of lattice cells and the solid line shows the interface).

$$g_i^{neq}(C_b, t) = -g_{i'}^{neq}(C_b, t) \; i = 3, 6, 7 \tag{12}$$

which leads to:

$$g_i(C_b, t) = -g_{i'}(C_b, t) + g_i^{eq}(C_b, u_b) + g_{i'}^{eq}(C_b, u_b) \tag{13}$$

where $u_b$ is the boundary node velocity assumed to be zero for a stagnant solid phase.

### 2.1.2. Hydrodynamic boundary treatment

In this study, two different hydrodynamic boundary schemes, including the standard bounce back (BB) scheme (He et al., 1997) and a curved boundary method (Chun and Ladd, 2007), were employed. In the BB scheme, the populations that leave the fluid node and enter the solid node are reflected at the wall surface to their original location in a one-time step. Defining the propagation step as:

$$f_i(x + c_i\Delta t, t + \Delta t) = f_i^{'}(x, t) \tag{14}$$

the corresponding BB boundary condition can be expressed as:

$$f_{i'}(x_{fb}, t + \delta t) = f_i^{'}(x_{fb}, t) \tag{15}$$

where $f^{'}$is the post-collision distribution function, $i^{'}$is the reverse direction of i, and $x_{fb}$ is a fluid node. Note that although the BB scheme is simple and efficient, it has two major drawbacks. First, it does not accurately reconstruct a smooth boundary curvature and a stepwise wall is used for the approximation. Secondly, several studies (Bouzidi et al., 2001; Li and Maa, 2017; Ma et al., 2017) have shown that using the common BGK collision operator, the position of the walls is not fixed by a BB constraint and their imposed locations would be a function of the value adopted for the relaxation time. This usually leads to the so-called viscosity-dependent permeability problem (Ginzburg and d'Humières, 2015; Ginzburg and D'Humières, 2003). These drawbacks were addressed by proposing curved boundary schemes (Chang et al., 2009; Guo et al., 2002; Kao and Yang, 2008; Yu et al., 2003). However, these schemes are not local and are computationally less efficient, and often require at least two nodes between near solid surfaces to reconstruct the smooth curvature of the interfaces. Among these methods, the

interpolation approach proposed by Chun and Ladd (2007) requires a minimum of one grid spacing between the nodes. Thus, this method was employed for curved boundary treatment in this study.

Chun and Ladd (2007) suggested an interpolation scheme that uses the distance between the fluid node and the wall (shown by q in Fig. 2) together with the values of the neighboring distribution functions to obtain the unknown distributions. Note that here the employed node type classification for hydrodynamic boundary condition is slightly different from that presented in Section 2.1.1, and the node is called quasi-solid if the volume of the lattice cell is greater than 0.5 and it is a quasi-fluid node if the volume is lower than 0.5. A boundary node ($x_{fb}$) on which the boundary condition is imposed is either a quasi-fluid node or a fluid node with at least one quasi-solid node in its neighborhood (e.g., node A in Fig. 2). Thus, for the fluid boundary nodes, the unknown distributions are those that come from quasi-solid nodes, and for quasi-fluid nodes, the unknown distribution functions are those that arise from solid or quasi-solid nodes.

Based on formulations shown in Fig. 2, the linear interpolation model of Chun and Ladd (2007) is formulated as follows:

$$f_{i'}^{eq}(x_{fb}, t+\Delta t) = 2q\, f_i^{eq}(x_{fb}, t) + (1-2q) f_i^{eq}(x_{fb} - c_i, t) \quad \text{for } q < \frac{1}{2} \tag{16}$$

$$f_{i'}^{eq}(x_{fb}, t+\Delta t) = \frac{1-q}{q} f_i^{eq}(x_{fb}, t) + \frac{2q-1}{q} f_i^{eq}(x_w, t) \quad \text{for } q \geq \frac{1}{2} \tag{17}$$

$$q \equiv \frac{|x_{fb} - x_w|}{|c_i|} \tag{18}$$

where $f_i^{eq}(x_w, t) \equiv f_i^{eq}(\rho_w, u_w)$, and the density at the surface, $\rho_w$, is considered as the average fluid density. After computing the equilibrium terms of the unknown distribution functions, the nonequilibrium distributions are obtained from the bounce-back rule (He et al., 1997).

$$f_{i'}^{neq}(x_{fb}, t+\Delta t) = f_i^{neq}(x_{fb}, t) \tag{19}$$

Often in LBM studies with curved boundary treatment, unchanging solid geometries are considered and therefore fixed values were assigned to q (Guo and Zhao, 2002; Izam et al., 2011; Mei et al., 2002; Xu et al., 2016). However, in dissolution problems, the two-phase interface changes over time and therefore q values should be recalculated and used for boundary treatment throughout the simulation. Therefore, the curved boundary method cannot be employed independently and should be coupled with surface tracking techniques. This issue is addressed in Section 3.1 and the method of calculating q instantaneously is presented.

### 2.2. Volume of fluid

Efficient reconstruction and tracking of the boundary between two contacting phases are challenging (Martinez et al., 2006; Pilliod and Puckett, 2004). The volume of fluid (VOF) is an effective approach for this purpose where the concept of fractional volume (V) is used and the two-phase interface in each cell is linked to this quantity. Detail reviews of coupling approaches are available in the literature (Pilliod and Puckett, 2004; Rudman, 1997; Scardovelli and Zaleski, 1999). An early algorithm of VOF was introduced by Noh and Woodward (1976). This method, which is known as simple line interface calculation (SLIC), neglects the possible orientation of the boundary and simply reconstructs the interface as a horizontal or vertical line (see Fig. 3 (a)). To address this drawback, more modern surface reconstruction methods -known as piecewise-linear methods-were introduced in the next years. Generally, in these methods, the interfaces are approximated as line segments with arbitrary slopes (Fig. 3 (b)). Youngs's method (1984) and the least-squares volume-of-fluid interface reconstruction algorithm (LVIRA) of Pilliod and Puckett (2004) are two common approaches of this type. In these methods, the position of the boundary is defined as a function of the orientation of the interface and the volume of the cell. However, as shown in Fig. 3 (b) these methods also suffer from discontinuity of interface segments. Although LVIRA minimizes such discontinuities, this is achieved at an expense of more complex algorithms and more computational costs compared to Youngs's model. For this study, both approaches were tested and since only marginal differences were observed between the results, the method of Youngs (1984) was employed and therefore is explained as follows.

As pointed out, for approximating the boundary interfaces as piecewise linear segments, the orientation of the interface should be calculated. Different methods (Martinez et al., 2006; Osher and Sethian, 1988; Pilliod and Puckett, 2004; Rudman, 1997) have been proposed for this purpose. The proposed method of Kothe (1991) has shown efficiency and therefore is used here. Assuming fractional volume as the ratio of the volume of the solid phase to the total volume of the cell (V), the vector of normal ($\boldsymbol{n}$) to the interface segment is defined as (Kothe, 1991):

$$n = \nabla V \tag{20}$$

According to Kothe (1991), to find the normal vector at the center of a cell, the normal vectors at the four neighboring vertices should be calculated first. For example for the cell of Fig. 4, discretization of Eq. (20) for the normal at (i+1/2, j+1/2) gives (Martinez et al., 2006):

$$n_{i+\frac{1}{2},j+\frac{1}{2}} = \left\{ \frac{(V_{i+1,j+1} - V_{i,j+1})\delta y_j + (V_{i+1,j} - V_{i,j})\delta y_{j+1}}{(\delta y_j + \delta y_{j+1})\delta x_{i+1}/2} \right\} \hat{i} + \left\{ \frac{(V_{i+1,j+1} - V_{i+1,j})\delta x_i + (V_{i,j+1} - V_{i,j})\delta x_{i+1}}{(\delta x_i + \delta x_{i+1})\delta y_{j+1}/2} \right\} \hat{j} \tag{21}$$

where V is the solid volume of a cell with a lattice node in the center. By averaging the normal at the four vertices, the normal at the cell center is calculated. For a uniform mesh with $\delta x = \delta y = 1$, the normal vector of the cell (i,j) is obtained from Eq. (21) (Martinez et al., 2006)

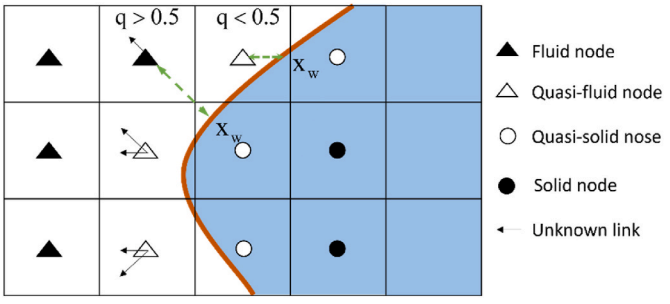


**Fig. 2.** Definition of different node types and their unknown directions in distribution functions.

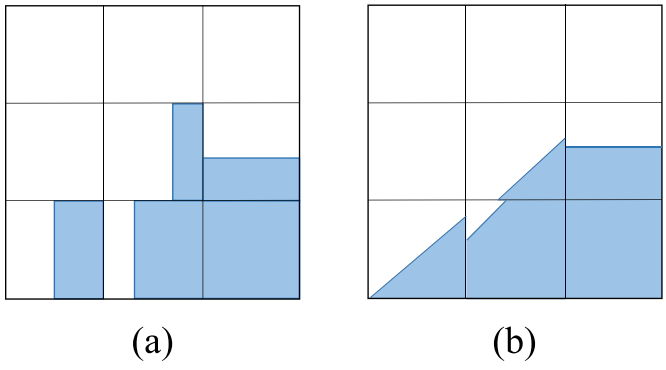


**Fig. 3.** Interface reconstruction by VOF method (a) SLIC, and (b) piecewise linear approximation.

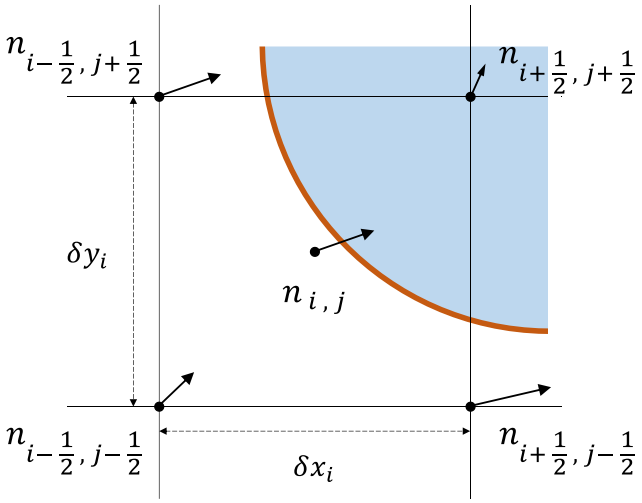


**Fig. 4.** Normal vectors at the four neighboring vertices of a cell.

$$\begin{aligned} n_{i,j} = &-\left(V_{i+1,j+1} + 2V_{i+1,j} + V_{i+1,j-1} - V_{i-1,j+1} - 2V_{i-1,j} - V_{i-1,j-1}\right)\hat{i} \\ &-\left(V_{i+1,j+1} + 2V_{i,j+1} + V_{i-1,j+1} - V_{i+1,j-1} - 2V_{i,j-1} - V_{i-1,j-1}\right)\hat{j} \end{aligned} \quad (22)$$

where$n_{i,j}$is multiplied by $-1$ to point toward the fluid domain. Having found the normal, the slope of the interface is obtained as:

$$\theta_{i,j} = \tan^{-1}\left(\left|\frac{n_x(i,j)}{n_y(i,j)}\right|\right) \quad (23)$$

where$\theta_{i,j} \leq 90$. Once the slope of the interface is found, the interface location can be calculated. In total, depending on the volume of the solid phase and the orientation of the interface, six possible interface types can be considered, as shown in Fig. 5.

Having found the slope and position of the interface, the specific surface area can be calculated. After calculating the solid volume fraction of the cell and the orientation of its interface, the corresponding interface configurations (shown in Fig. 5) determine values for x and y coordinates. Finally, the surface area can be calculated by the Pythagorean theorem as $a_v = \sqrt{x^2 + y^2}$.

## 3. Simulation procedure

In studies that have applied the curved boundary method, the solid phases seldom evolved over time; thus, the solid-fluid interfaces were static and q values were fixed. However, for evolving geometries, the values of q are continuously changed and should be recalculated in each iteration. As described in Section 2.2, this can be achieved by a combination of VOF and curved boundary methods. The conditions for VOF employment in LBM framework are formulated in Section 3.1, where the derivation methods are explained and the necessary relations for curved boundary-VOF combination are presented.

For investigating the performance of the volume of pixel method (VOP), we perform simulations under different dissolution regimes and compare the results with VOF for both simple and complex media (in Sections 4.1 and 4.2, respectively). For this purpose, simulation of calcium carbonate dissolution by hydrochloric acid is considered. After this, we continue by comparing the performance of the curved boundary scheme with the bounce back approach under different dissolution regimes. While the bounce back approach approximates the boundaries as staggering steps, the curved boundary scheme accurately reconstructs the smooth curvature of the solid interfaces, though at the expense of higher computational costs and employing more complex algorithms. Thus, a comparison of both approaches for the dissolution process is studied in Sections 4.1 and 4.2 for both simple and complex media, respectively.

### 3.1. VOF formulation and its combination with the curved boundary method

Alteration of the solid phase in heterogeneous reactions is proportional to the reaction flux at the interface. The solid mineral volume evolution can be calculated by (Chen et al., 2015):

$$\frac{\partial V(X_b,t)}{\partial t} = -V_m a_v R \quad (24)$$

where $X_b$is the position of boundary nodes (i.e., quasi-fluid and quasi-solid nodes), V is the volume fraction of the dissolved solid phase, $V_m$ is the molar volume of the solid phase, $a_v$ is the specific surface area, and R is the reaction flux. For dissolution and precipitation processes, R takes positive and negative values, respectively. The value of V is updated explicitly at each time step as (Chen et al., 2015):

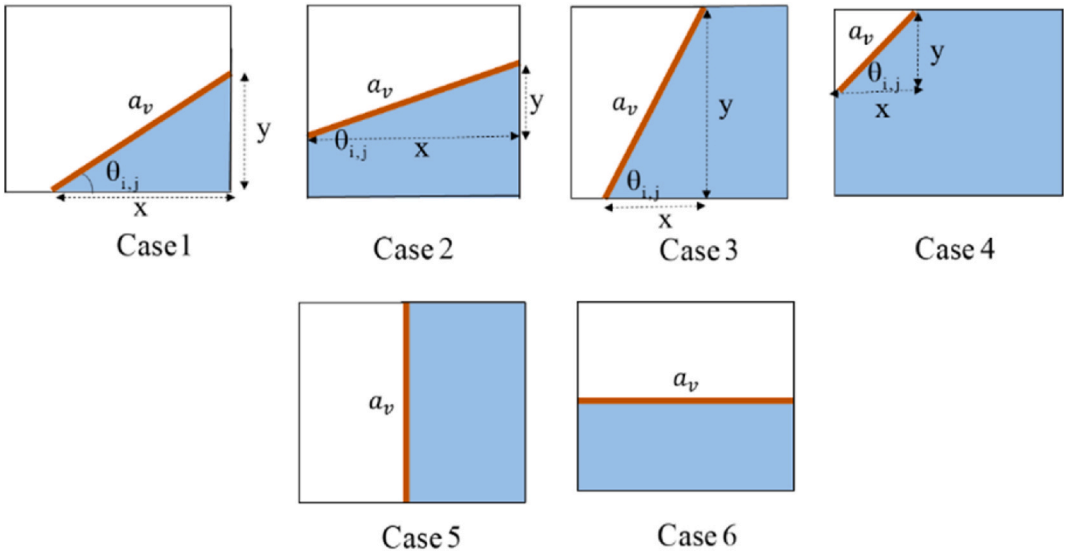


**Fig. 5.** Possible configurations depend on interface orientation and the solid fraction of the cell. The red color lines indicate the interfaces and the shaded parts represent the solid phase. (For interpretation of the references to color in this figure legend, the reader is referred to the Web version of this article.)

$$V(X_b, t+\Delta t) = V(X_b, t) - V_m a_v R \Delta t \tag{25}$$

The specific surface area, $a_v$, changes with the evolution of the solid phase. However, often LBM simulations neglect the dynamic change of $a_v$ and assume a value of one for simplicity. In this study, for instantaneous calculation of $a_v$ the volume of fluid method (described in Section 2.2) is employed. However, the common approach for calculating $a_v$ and q (in the curved boundary method) can be rather complicated and therefore studies often apply the VOP method by setting $a_v = 1$ and using the conventional bounce-back boundary condition rather than applying the curved boundary scheme.

Considering the six configurations shown in Fig. 5 the procedure includes 1) Checking the neighboring cells and finding the normal vector from Eqs. (22) and (2)) calculating the slope of the interface from Eqs. (23) and (3)) assuming the solid phase to have a right-angled triangle shape, the interface slope and Pythagorean theorem is used to find the x and y values (shown in Figs. 5), 4) using the conditional terms in Eq. (26) to determine the interface configurations, 5) calculating the interface area using Eq. (27).

$$\begin{aligned}
&0 < \theta_{i,j} \le 45 \begin{cases} V_{i,j} \le 0.5 \begin{cases} (x\&y) \le 1 \rightarrow \text{case 1} \;\; \alpha = 1 \,, (\beta, \lambda, \gamma) = 0 \\ \text{else} \rightarrow \text{case 2} \;\; \lambda = 1 \,, (\alpha, \beta, \gamma) = 0 \end{cases} \\ 0.5 < V_{i,j} < 1 \begin{cases} (x\&y) \le 1 \rightarrow \text{case 4} \;\; \beta = 1 \,, (\alpha, \lambda, \gamma) = 0 \\ \text{else} \rightarrow \text{case 2} \;\; \lambda = 1 \,, (\alpha, \beta, \gamma) = 0 \end{cases} \end{cases} \\
&45 < \theta_{i,j} < 90 \begin{cases} V_{i,j} \le 0.5 \begin{cases} (x\&y) \le 1 \rightarrow \text{case 1} \;\; \alpha = 1 \,, (\beta, \lambda, \gamma) = 0 \\ \text{else} \rightarrow \text{case 3} \;\; \gamma = 1 \,, (\alpha, \beta, \lambda) = 0 \end{cases} \\ 0.5 < V_{i,j} < 1 \begin{cases} (x\&y) \le 1 \rightarrow \text{case 4} \;\; \beta = 1 \,, (\alpha, \lambda, \gamma) = 0 \\ \text{else} \rightarrow \text{case 3} \;\; \gamma = 1 \,, (\alpha, \beta, \lambda) = 0 \end{cases} \end{cases} \\
&\theta_{i,j} = 90 \rightarrow \text{case 5} \;\; \gamma = 1 \,, (\alpha, \beta, \lambda) = 0 \\
&\theta_{i,j} = 0 \rightarrow \text{case 6} \;\; \lambda = 1 \,, (\alpha, \beta, \gamma) = 0
\end{aligned} \tag{26}$$

$$a_v^2(X_b, t) = \frac{2}{\tan\theta}\left(1 + \tan^2\theta\right)\left[\alpha V(x_b, t) + \beta(1 - V(x_b, t))\right] + \gamma\left(1 + \frac{1}{\tan^2\theta}\right) + \lambda\left(1 + \tan^2\theta\right) \tag{27}$$

where coefficients $\alpha, \beta, \lambda$ and $\gamma$ are calculated in step 4 where depending on the signs of $n_x$ and $n_y$ 4 variations are possible. Such variations for case 2 are shown in Fig. 6. Similarly, two variations can be considered for cases 5 and 6.

So far, the procedure for implementing the piecewise linear VOF is explained. The bounce back or other approximating boundary conditions considering interface steps can be independently combined with this method with no further treatments. However, when accurate reconstruction of boundary curvatures is desired, special curved boundary schemes should be implemented which adds extra complexity to the algorithms. In reactive flows, where the interface location continuously changes, q values should be calculated in each iteration by intersecting discrete velocity lines, where the interface line segment is calculated using the VOF method. Hence, mathematical relations should be constructed for the interface line to find $x_w$ and q for Eqs. (16)–(18). For this purpose, after determining the boundary node type, the intersection points of the interface line with cell boundaries should be found. In appendix A, an example of q calculation is given.

Clearly, the combination of VOF methods with curved boundary schemes would be more complex than their coupling with step boundary schemes such as the common bounce back method. This is mainly due to the fact that the curved boundary schemes require all q values in all discrete velocity directions to be accurately determined in each time step. However, methods such as the common bounce back assume one lattice unit distance between the interface and all neighboring fluid nodes and hence circumvent the steps required to determine line equations and their intersections. Hence, they generally offer more simplicity, but at the risk of lower accuracy. Further, an intermediate approach is investigated in this study to look for a tradeoff between the acquired accuracy and the computational costs. One option is to approximate the distance between the interface and the neighboring fluid nodes as a function of the solid content of the cell, i.e.:

$$q = 0.5 + [a - V(X_b, t)] \begin{cases} a = 1 & (\text{If } X_b \text{ is a quasi} - \text{solid node}) \\ a = 0 & (\text{If } X_b \text{ is a quasi} - \text{fluid node}) \end{cases} \tag{28}$$

This implies that the value of q can be estimated as a function of the type of the boundary node and its solid volume fraction. This approach neither requires the determination of the interface lines nor their intersections with discrete velocity lines.

### 3.2. Problem statement

The performance of VOP and VOF methods and their combination with BB and curved boundary schemes in dissolution regimes was studied by simulation of the reaction of calcium carbonate with hydrochloric acid. The simulation results are compared between the two methods. We have considered two different media, one being a simple media (Fig. 7) and one a more complex domain (Fig. 8). For both cases, the mineral interface was assumed to undergo the following irreversible

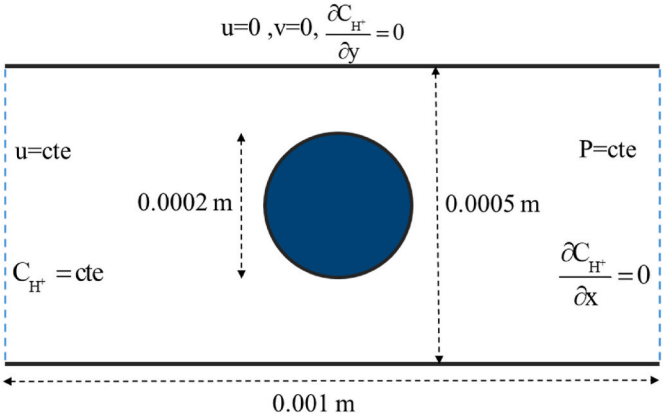


**Fig. 7.** Simulated geometry and the applied boundary conditions to compare the performance of VIP and VOF methods using a simple flow domain.

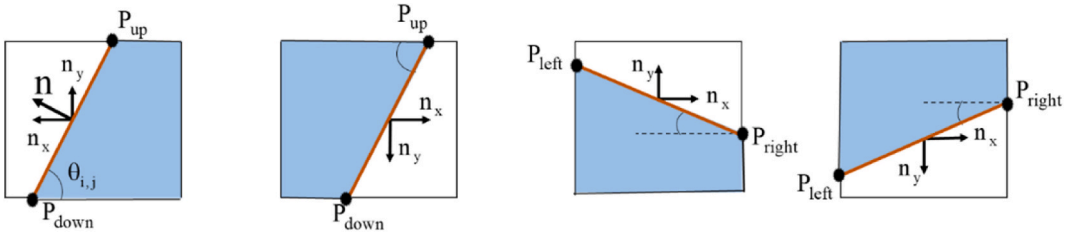


**Fig. 6.** Variations for case 2 depend on the signs of $n_x$ and $n_y$. P denotes the intersection of the interface with cell boundaries.

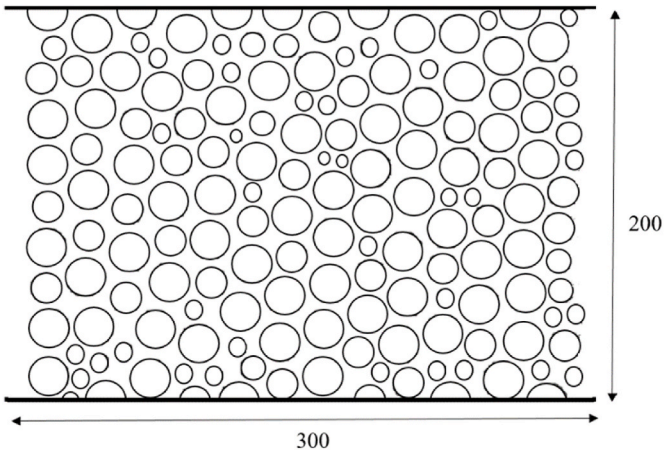


**Fig. 8.** Porous media geometry with an initial porosity of 42% was used as a complex pore structure to compare the performance of the VOP and VOF methods.

heterogeneous reaction:

$$CaCO_3(s) + H^+ \rightarrow Ca^{2+} + HCO_3^- \tag{29}$$

Considering a first-order reaction rate as a function of the $H^+$concentration provides:

$$r = k_{H^+}\gamma_{H^+}C_{H^+} \tag{30}$$

A comparison between Eqs. (30) and (10) shows that $k_r = k_{H^+}\gamma_{H^+}$and $C_b = C_{H^+}$, where $k_{H^+}$and $\gamma_{H^+}$are reaction rate constant and activity coefficient, respectively. As the instantaneous rate of carbonate dissolution depends only on $H^+$concentration, the multicomponent species system can be computationally reduced to a single component transport problem for $H^+$ion transport.

The simulation for the simple case (Fig. 7) in this study is similar to the benchmark problem reported in Molins et al. (2020). In their work, they have performed simulations using five different solvers, i.e., OpenFOAM-DBS, Chombo-Crunch, a lattice Boltzmann code, Vortex, and dissolFoam and have compared the results. Fig. 7 shows their simulated domain and their employed boundary conditions (Molins et al., 2020). The problem mainly regards the injection of hydrochloric acid into a channel with a calcium carbonate mineral located in the center. For acid flow, a uniform velocity at the inlet, a fixed pressure boundary condition at the outlet and a no-slip boundary condition at lateral walls were applied using the Zou and He method (1997). For concentration, the approach of Zhang et al. (2012) was used to impose Dirichlet and Neumann boundary conditions at the inlet and outlet faces, respectively. The concentration flux across the lateral walls is set to zero and a Robin boundary condition (Eq. (10)) at the fluid-solid interface is applied (Zhang et al., 2012).

For finding the appropriate mesh size, the grid independency was checked and $128 \times 256$ mesh size was found as the optimum resolution (detailed results not presented here). Table 1 provides the physical and LBM unit values of the parameters used for the simulation of the dissolution process in the simple domain.

In engineering applications of porous media, precise tracking of the evolution of individual grains is seldom the primary goal and they aim at finding average quantities such as porosity, permeability, and the dissolution pattern. It is possible that while a given algorithm shows weakness in accurately tracking the evolution of a single grain, it still offers acceptable performance in simulating medium-averaged quantities. Accordingly, in addition to the described single grain problem, the problem of pore scale dissolution in a porous medium was also examined in this study. A porous structure with an initial porosity of 42% is used as shown in Fig. 8. The applied boundary conditions were similar to those

**Table 1**
The physical and LBM unit values of parameters used for the dissolution simulation of a single carbonate grain in a simple domain.

| Parameter | Symbol | Physical value | LBM value |
|---|---|---|---|
| Width of channel | w | $0.05 \times 10^{-2}$m | 128 |
| Length of channel | L | 0.001 m | 256 |
| Radius of grain | R | 0.0001 m | 25.6 |
| Fluid density | $\rho$ | 1000 kg/m$^3$ | 1 |
| Kinematic viscosity | $\vartheta$ | $10^{-6}$ m$^2$/s | 0.167 |
| Diffusion coefficient | D | $10^{-9}$ m$^2$/s | $1.67 \times 10^{-4}$ |
| Inlet velocity | u | 0.0012 m/s | $7.8 \times 10^{-4}$ |
| Inlet concentration | $C_{H^+}$ | 10 mol/m$^3$ | $10^{-5}$ |
| Reaction rate constant | $K_{H^+}$ | $10^{-0.05}$ mol/m$^2$s | $5.8 \times 10^{-4}$ |
| Activity coefficient | $\gamma_{H^+}$ | $10^{-3}$ m$^3$/mol | 1 |
| Calcite molar volume | $V_m$ | $36.9 \times 10^{-6}$m$^3$/mol | 36.9 |
| Reynolds number | $Re = \frac{uw}{\vartheta}$ | 0.6 | 0.6 |
| Peclet number | $Pe = \frac{uw}{D}$ | 600 | 600 |
| DamKöhler number | $Da = \frac{K_{H^+}\gamma_{H^+}2R}{D}$ | 178 | 178 |

used for the single grain problem. Since the pattern of dissolution in porous media depends on various governing dimensionless numbers (Fredd and Fogler, 1998; Jiang et al., 2021; Mostaghimi et al., 2016; Taahodi et al., 2021) and in order to maintain the generality of the problem, simulations were conducted under two different regimes. Values for Peclet and DamKöhler numbers were chosen so that face dissolution and uniform dissolution patterns could be investigated. Table 2 provides the dimensionless numbers used for reactive porous medium simulation.

## 4. Results and discussion

### 4.1. Validation of the algorithms

For validating the algorithms developed for this work, the results from reactive transport using the simple geometry were compared with the findings reported by Molins et al. (2020). For comparison purposes and to keep similarity between this work and that of Molins et al. (2020), the shape and solid content of the grain were assumed constant and thus the gradual volume reduction of the solid grain was neglected. Hence, convergence into a steady-state flow and concentration field is expected. Fig. 9 (a) displays the steady-state contours of $H^+$concentration and Fig. 9 (b) illustrates pH values along horizontal and vertical centerlines ($x = 5 \times 10^{-4}$ m, $y = 2.5 \times 10^{-4}$ m), where $pH = -log(\gamma_{H^+}C_{H^+})$. Since the diffusion coefficient was low, a thin boundary layer forms around the grain as shown in Fig. 9 (a). Sharp consumption of $H^+$ is well displayed in Fig. 9 (b). Comparison of the results shows an excellent agreement between the results of the present work and those of Molins et al. (2020).

### 4.2. Dissolution of a single grain

The performance of VOP and VOF methods as well as their combination with bounce-back and curved boundary schemes were investigated for the problem of the single grain dissolution under four different scenarios, where: 1) surface of dissolution was tracked by VOF with

**Table 2**
Dimensionless numbers and their values were used for reactive porous medium simulation.

| Dimensionless numbers | Face dissolution | Uniform dissolution |
|---|---|---|
| $Re = \frac{uw}{\vartheta}$ | 0.2 | 0.2 |
| $Pe = \frac{uw}{D}$ | 0.065 | 6.5 |
| $Da = \frac{K_{H^+}\gamma_{H^+}w}{D}$ | 10 | 0.01 |

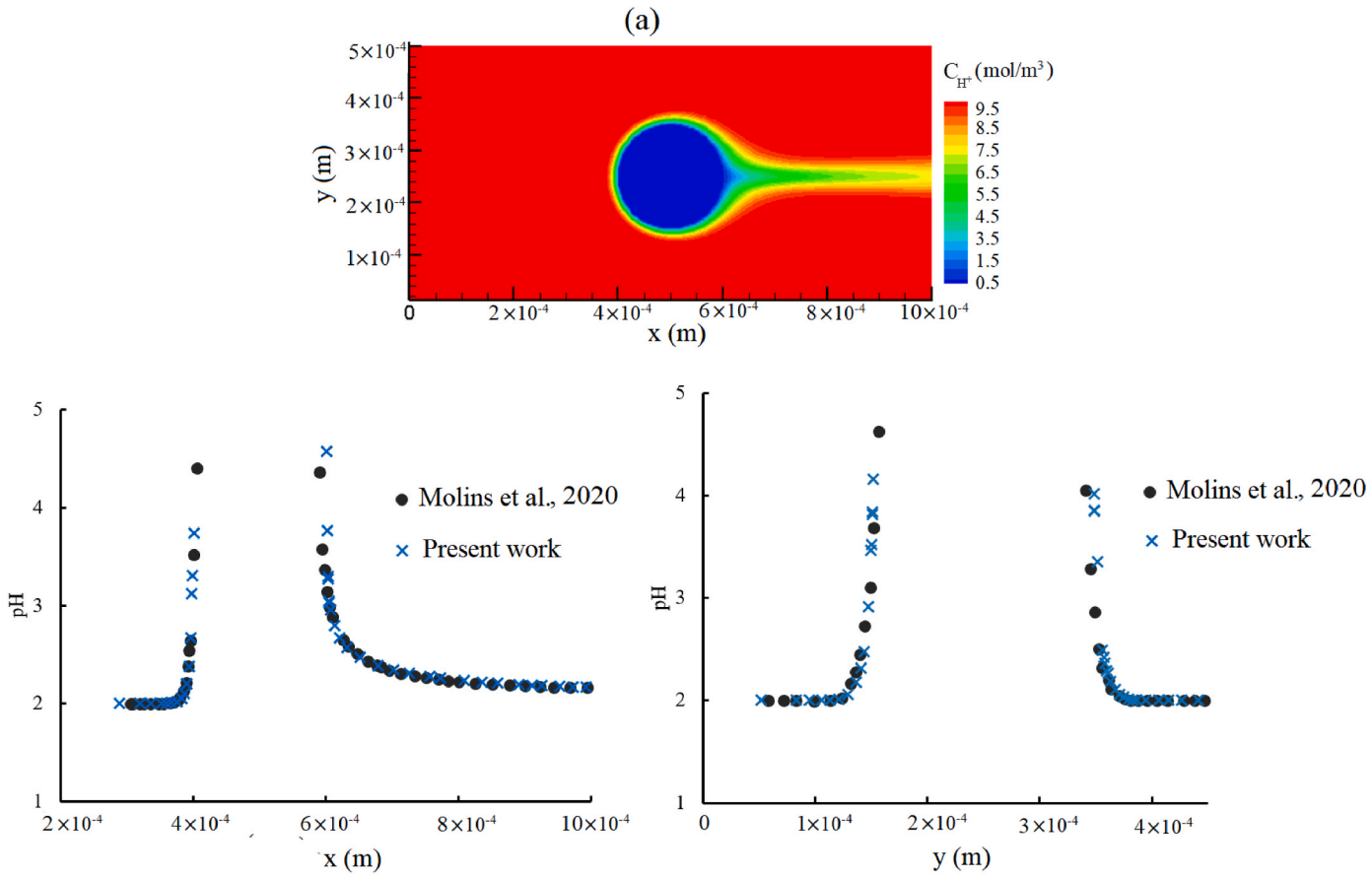


**Fig. 9.** (a) Contour of $H^+$ concentration (b) the left and the right figure show pH values along horizontal and vertical centerline respectively.

bounce-back used as the hydrodynamic boundary condition, 2) surface of dissolution was tracked by VOF with curved boundary approach employed for the hydrodynamic boundary condition, 3) surface of dissolution was tracked by VOF with an approximate curved boundary approach (Eq. (28)) utilized for the hydrodynamic boundary condition, and 4) no surface tracking technique was employed (i.e., the VOP approach) with bounce-back applied as the hydrodynamic boundary condition. As the comparison of curved and step hydrodynamic boundary conditions as well as the study of their impacts on momentum and velocity fields have been the subject of several previous studies (Chun and Ladd, 2007; Ginzburg, 2005b; Mei et al., 2002; Xu et al., 2016; Yu et al., 2003) in this study we focus on their impacts on reaction characteristics and concentration fields.

The initial radius of the grain was set $10^{-4}$ m, which corresponds to the initial area of $6.28 \times 10^{-6}$ $m^2$. Injection of acid into the channel causes gradual dissolution of the carbonate grain with its surface area diminishing over time. Fig. 10 displays the variations of the surface area with time for the four mentioned scenarios. Since Molins et al. (2020) concluded that the OpenFOAM-DBS method had the least deviation from the experimental data, their OpenFOAM-DBS results, in addition to

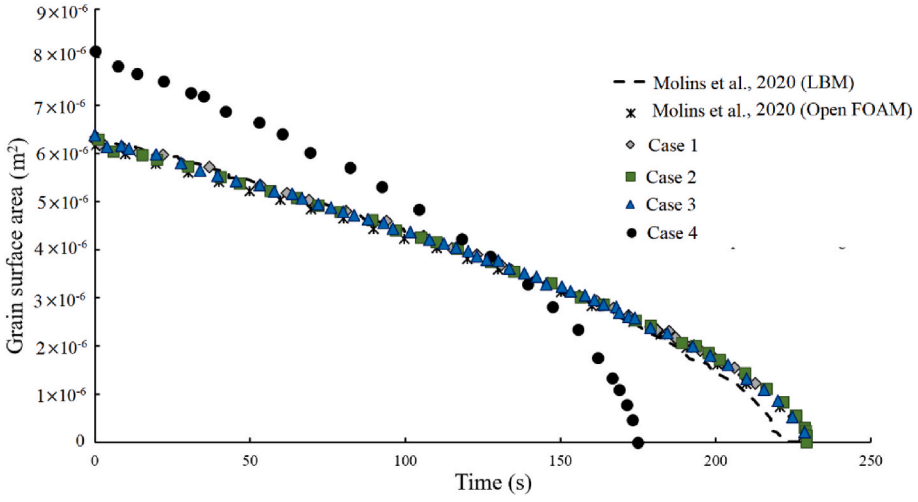


**Fig. 10.** Variation of the dissolving grain's surface area with time for the 4 different scenarios.

their LBM findings, are presented in Fig. 10 to make comparisons with our simulations. Fig. 10 indicates that scenarios 1, 2, and 3 where instantaneous reaction area was tracked, provided a good agreement with the results of Molins et al. (2020). However, for the fourth scenario, the time variation of the surface area shows a different trend and with sharper gradients. Indeed, despite the larger value calculated for the initial surface area of the fourth scenario (29% more than the real value), its value diminished more rapidly, particularly as the grain became smaller. This is mainly because at the later stages of dissolution of a boundary cell, although the specific surface area of the cell would be almost zero yet (unless the entire solid content of the cell is dissolved), the VOP method would assign a fixed value of 1 to this variable. Hence, it causes a higher rate of dissolution by VOP. Fig. 10 also indicates that the type of hydrodynamic boundary condition would not have a major influence on the instantaneous values of the total surface area of the dissolving grain.

Furthermore, for comparing the geometrical evolutions, the total surface area is shown versus medium porosity in Fig. 11 (a). As depicted in Fig. 11 (a), while the calculated surface areas of scenario 1, 2 and 3 are essentially similar, the calculated values for scenario 4 is almost always higher than the other cases. However, upon increasing porosity the difference gradually decreases, suggesting by once the solid volume diminishes, the absolute difference between the VOF and VOP methods becomes smaller. To further scrutinize this observation, plots of the absolute difference and relative percent difference between the surface area of VOP and VOF methods are presented in Fig. 11 (b). Although with increasing porosity, the absolute difference between the two methods decreases, this reduction cannot be interpreted as an indication of increased accuracy for VOP method and in fact this is mainly due to the smaller number of pixels being analyzed. This argument is supported by the plot of a relative percent difference, which reveals that generally the VOP method approximates the surface area about 30% higher than the VOF method does.

Note that due to the different approaches employed by the VOP and VOF methods for the surface area calculation, unequal values are observed for the grain's initial surface area in Figs. 10 and 11. While the VOF method approximates the interface as piecewise linear segments and uses it to calculate the surface area of every individual interface node, VOP maps the geometry into a staggering step body and assumes each interface node to have surface area of unity. The latter approach, despite its simplicity, overestimates the surface area, thus leading to higher volume reduction rates in comparison to VOF (see Appendix B for more details).

In addition, the time-averaged surface area ($\overline{A}$) for the dissolving grain from the initial time to the moment of complete disappearance is calculated by $\overline{A} = \int A(t)dt \,/\Delta t$. The $\overline{A}$ calculated using VOF and VOP has been $3.93 \times 10^{-6}$ m$^2$ and $5.18 \times 10^{-6}$ m$^2$, respectively. Assuming the VOF results as the more accurate values, the comparison reveals that for the circle geometry, VOP overestimates the surface by 32%.

Due to the different approaches of VOP and VOF methods in handling surface area and their similarities in volume calculations, a comparison of the methods from a volumetric perspective is useful. Variations of the grain's volume over time and its disappearance rate have been studied with Fig. 12 depicting the volume change from its initial value ($3.14 \times 10^{-10}$m$^3$) up to its complete disappearance. All cases started with the same initial value, while the volume reduction rate of scenario 4 was more pronounced with nearly 23% faster disappearance. The sharper trend in scenario 4 in comparison with the other cases indicates that the assumption of constant value of unity for reaction surface area would be (on average) relatively larger than the true physical value. The closeness of the other trends is in agreement with the results of Fig. 10, suggesting that the choice of hydrodynamic boundary condition would have no major impact on volumetric aspects of the dissolution.

In addition to surface and volume evolutions, the trends of average dissolution rate per unit area (R) are also depicted in Fig. 13. For this purpose, the volume changes of the grain at each time step were multiplied by its molar volume:

$$R = -V_m \frac{dV}{dt} \tag{31}$$

Fig. 13 (a) reveals the variations of dissolution rate versus porosity. The dissolution rate using the VOP method is always greater than that of the other three VOF cases, and clearly, the main cause is the difference in their corresponding surface area. As the VOP overestimates the surface area on which the heterogeneous reaction occurs, this method would in turn overestimate the average dissolution rates by a factor of $f = \overline{A}_{VOP}/\overline{A}_{VOF}$. Thus, if the dissolution rates are normalized by their corresponding surface area, essentially similar trends are expected for all cases, as confirmed by plot of Fig. 13 (b).

Fig. 13 (c) illustrates the variations of the average $H^+$ concentration at the outlet of the medium with variations of the porosity. At the early injection times, the concentration of $H^+$ at the outlet face grows sharply with the injection of $H^+$ at the inlet, after which the $H^+$ concentration gradually rises due to the decline in its rate of consumption. Fig. 13 (b) and (c) also show that the choice of concentration boundary conditions had no major effect on the concentration field. It could be argued that the differences observed between the results of VOP and VOF in previous

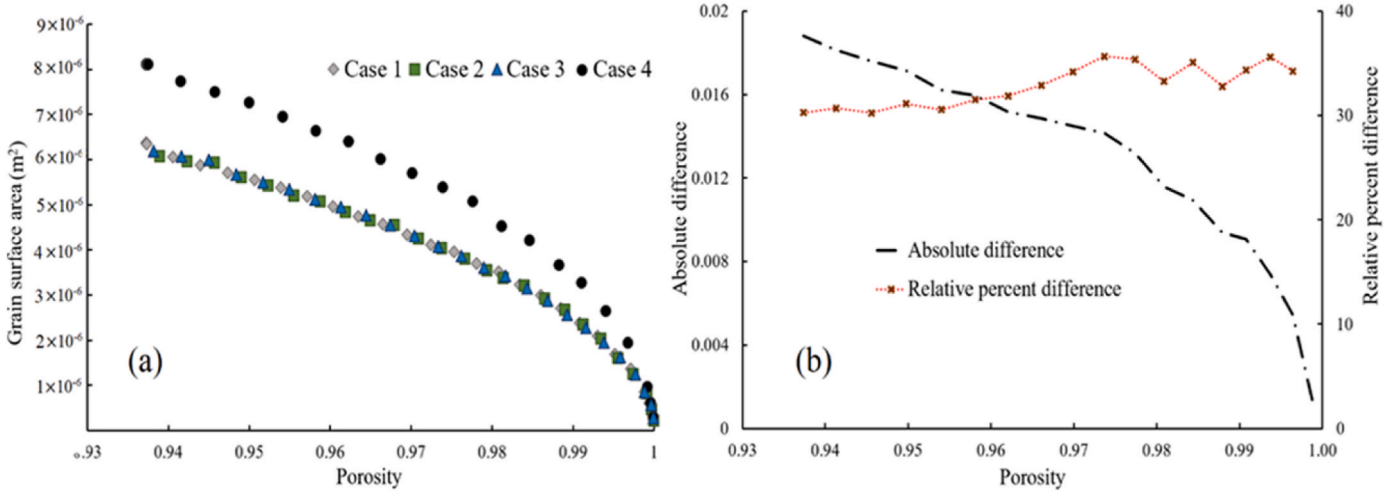


**Fig. 11.** (a) Variation of the grain's area by porosity for the 4 different methods (b) Relative percent difference and the absolute difference between the surface area values calculated by VOP and VOF methods.

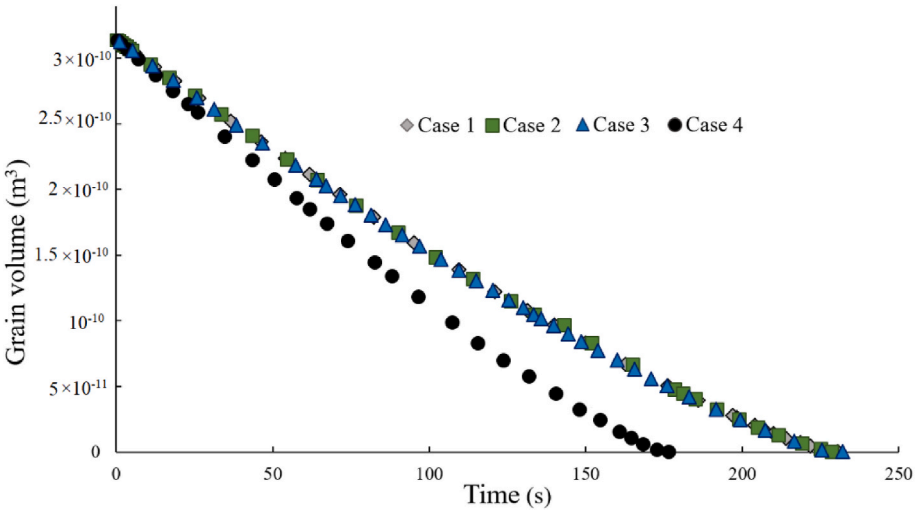


**Fig. 12.** Variation of the grain's volume over time for the 4 different scenarios.

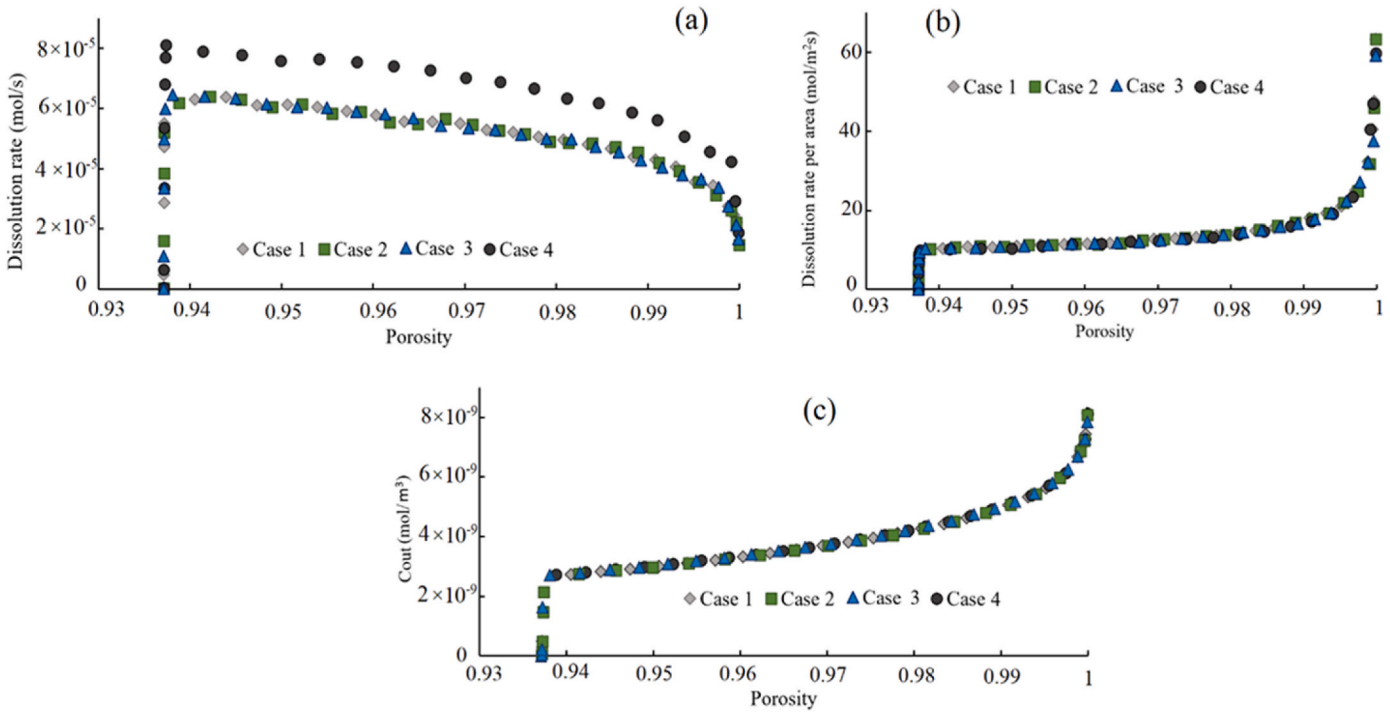


**Fig. 13.** Variation of (a) the dissolution rate (b) dissolution rate per area (c) the average outlet concentration with porosity changes.

figures could be (at least partially) due to their different method of concentration implementation on the grain's boundary. However, Fig. 13 disproves this possibility and shows the similarity of the two concentration boundary conditions.

Fig. 14 shows that an overestimation of 32% in surface area when using the VOP method has led to about 30% higher reaction rates and thus about 30% faster disappearance of the grain. In total, Figs. 10–14 indicate that the VOP method may heavily impact the temporal aspects of the dissolution problem, even though the non-temporal aspects are not impacted extensively.

For comparing the geometry evolutions for the four cases, grain profiles at the same values of solid volume are illustrated in Fig. 15. In this figure, $V_0$ is the initial volume of the solid phase. Although with progression of the dissolution, the differences between the geometries become more pronounced, to compare the performance of the methods, the complete evolutionary history of each case should be considered. As displayed in this figure, for volume magnitudes of $V_0/2$, $V_0/4$, and $V_0/8$, grain shapes for scenarios 1, 2, and 3 are nearly similar. However, the VOP application in scenario 4 has led to a less smooth shape with sharper edges, which could be due to the binary nature of the surface area in this method. Looking at the history of the geometry evolution of the solids, the solid shape of the simplified curved-boundary scenario (i.e., case 3) would be essentially similar to that of the original curved boundary method (i.e., case 2). The dissolution times of cases 1, 2, and 3 have no considerable difference. However, for case 4, shorter times are observed which is in agreement with the points noted on Figs. 10, 12 and 14.

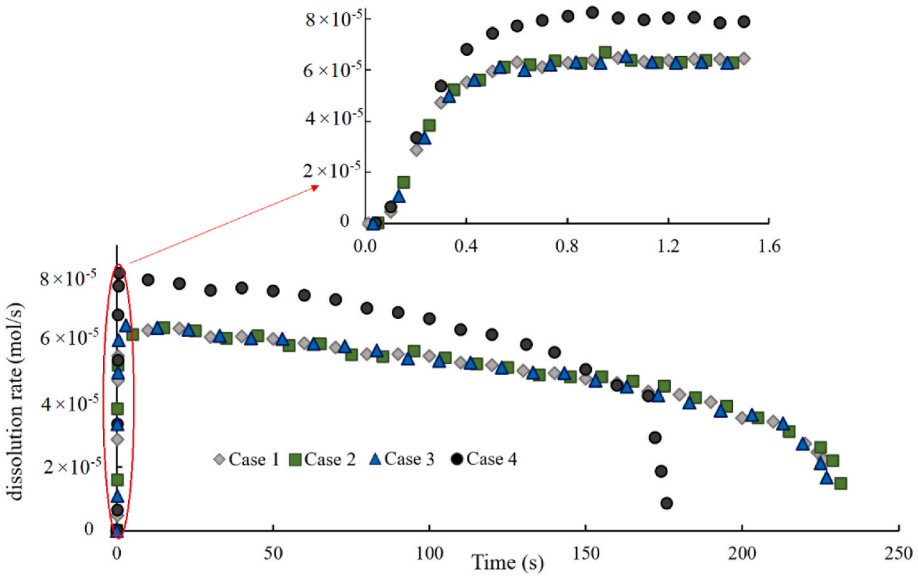


**Fig. 14.** Variation of the dissolution rate over time for the 4 different methods.

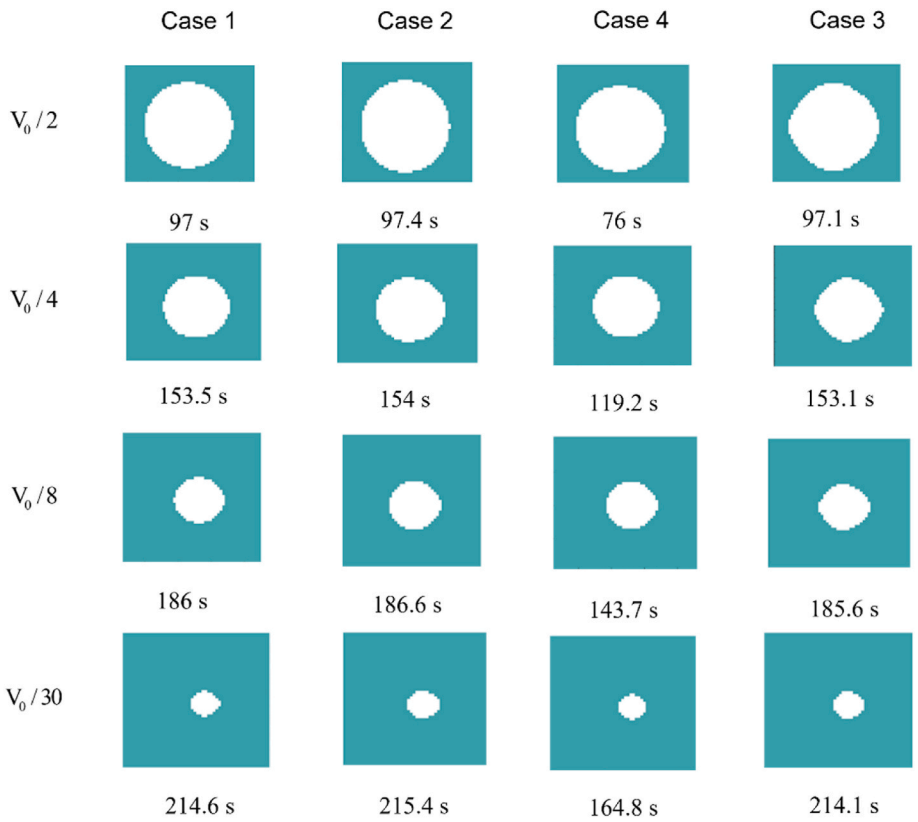


**Fig. 15.** Comparison of the grain's geometry evolution for the four different methods. The associated time of dissolution is provided below each profile.

### 4.3. *Dissolution of porous media*

In this section, we explore the simulation of reactive transport in complex porous media structure. Due to the substantially higher amounts of surface area in aggregated geometries, more pronounced averaged behavior is expected. Dissolution of porous media under two different regimes, named face dissolution and uniform dissolution regimes, are explored in this section. From surface area perspective, these two regimes lie on two opposite extremes. While the face dissolution mainly acts on the front face of the medium (and fewer grains are involved in dissolution) the uniform dissolution affects the whole medium simultaneously. For guaranteeing the development of these regimes, high Damköhler/low Peclet numbers (causing face dissolution) and low Damköhler/high Peclet numbers (causing uniform dissolution) should be maintained (Fredd and Fogler, 1998; Kang et al., 2003; Mostaghimi et al., 2016; Taahodi et al., 2021; You and Lee, 2021). In the two following subsections, the importance of tracking the solid-fluid interfaces in porous media and the choice of hydrodynamic boundary

conditions were investigated. Since comparison of the performance of the methods is the main goal of this section and physical interpretation of the underlying transport phenomena is not intended here, all outcomes of the simulations are presented in lattice units.

#### 4.3.1. Face dissolution regime

For comparing the 4 algorithms under the face dissolution regime, simulations were conducted at Pe = 0.065 and Da = 10 where low flow rate and high reaction rate prevent downstream dissolution before the front face is dissolved. Fig. 16 shows the dissolution patterns and simulation time steps at 60, 80, and 95% porosity values for the 4 cases. Results showed that despite some marginal geometrical differences, the observed face dissolution patterns for all cases are similar. However, the necessary time steps for the 4th case to reach the target porosities are considerably different from the other three cases. In other words, although the computation of the reactive area affected the temporal dissolution characteristics it had no clear effect on the dissolution patterns. Furthermore, results show that the choice of hydrodynamic boundary treatment (i.e., stair-step approximation or curved boundary) did not affect the dissolution pattern or the dissolution time. Therefore, the results demonstrate that despite the underlying approximation in the bounce-back method, this method provides nearly the same performance in comparison with the more accurate (but less efficient) curved boundary scheme.

Fig. 17 illustrates a temporal variation of the normalized porosity (Fig. 17 (a)), surface area (Fig. 17 (b)) and solid volume (Fig. 17 (c)) of the porous medium. Except for the 4th case, which shows a faster dissolution, all the other cases show similar evolution. As shown in Fig. 17 (b), although the initial surface area of case 4 was 25% more than that of the other three cases, the dissolution took place almost 23% faster due to the higher specific surface area considered in the VOP method. Therefore, in agreement with the previous results, employing the VOP method and neglecting the variation of solid-fluid interfaces may highly affect the temporal characteristics of the phenomenon of dissolution in porous media.

The non-temporal aspects of the dissolution problem are perused in Fig. 18 (a), in which trends of surface area as a function of porosity are illustrated. As the results of cases 1, 2 and 3 were similar, they are shown using one single plot labeled as VOF. The variation of surface area in the face dissolution regime shows an almost linear trend for both VOP and VOF methods. Similar to grain dissolution trends, the calculated surface area by VOP is always higher than that of the VOF method. However, by reduction of the volume of the solid phase (i.e., by increasing porosity) the surface area calculated by VOP becomes closer to that of the VOF method. This trend is illustrated in Fig. 18 (b) which shows that by increasing porosity the absolute difference between the trends of VOP and VOF becomes smaller while the VOP method still significantly (about 25%) overestimates the surface area.

Fig. 19 (a) shows the variation of dissolution rate (using Eq. (31)) over time for the 4 cases. No clear difference between the results of cases 1, 2 and 3 is observed. The overestimation of the surface area in case 4 has led to higher dissolution rates which in turn provides an almost 23% faster disappearance rate. Fig. 19 (b) shows the variation of dissolution rate versus porosity changes. For all porosities, the higher calculated area of case 4 (shown in Fig. 18 (a)) has led to higher dissolution rates. However, as it is illustrated in Fig. 16, face dissolution mainly operates at the front face of the medium and therefore a lesser amount of surface area is involved in the reaction. This causes the trend of dissolution rate of case 4 to be similar to that of the other cases in comparison with the uniform dissolution which affects the whole interface of the medium simultaneously (see Fig. 23 (b) for comparison). In Fig. 19 (c), the effect of the surface area is excluded by normalizing dissolution rates using the surface area. The agreement between trends shows that surface area creates the major reason for the deviation between the VOP and VOF methods and the choice of hydrodynamic boundary condition had no major impact on the transport of species in porous media.

#### 4.3.2. Uniform dissolution

Under a high Peclet/low Damköhler (Pe = 6.5 and Da = 0.01) regime, a reaction-limited transport (Mostaghimi et al., 2016) known as uniform dissolution is expected. In such dissolution regimes, almost all solid grains dissolve simultaneously and therefore in comparison with face dissolution a considerably larger number of grains would be involved in the reaction. Fig. 20 shows dissolution patterns and their corresponding time steps for all four cases for porosity values of 60, 80 and 95%. All cases show similar uniform dissolution patterns and only marginal differences can be observed between the shapes of some grains. However, the corresponding time steps for the 4th case are considerably different from the others which are mainly due to the higher specific surface area calculated by the VOP method. Therefore, similar to the face dissolution regime, a significant difference in temporal aspects of simulations is observed. Furthermore, results show that the choice of hydrodynamic boundary treatment did not considerably affect dissolution patterns or time steps and the results were similar.

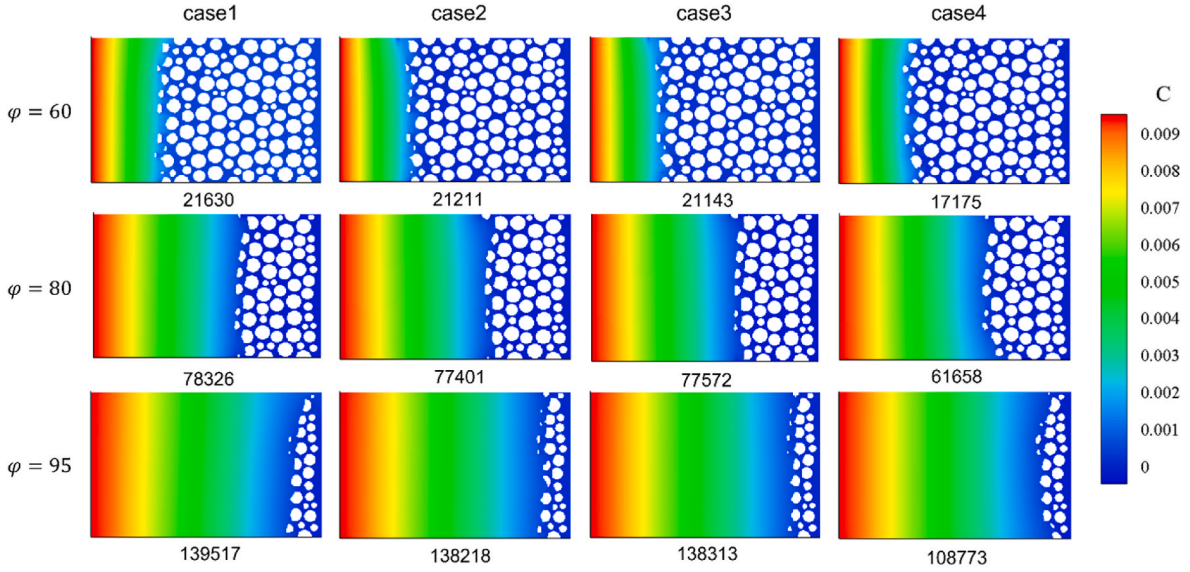


**Fig. 16.** Profiles of the dissolving porous medium at 60, 80, and 95% porosities for the 4 algorithms at Pe = 0.065 and Da = 10.

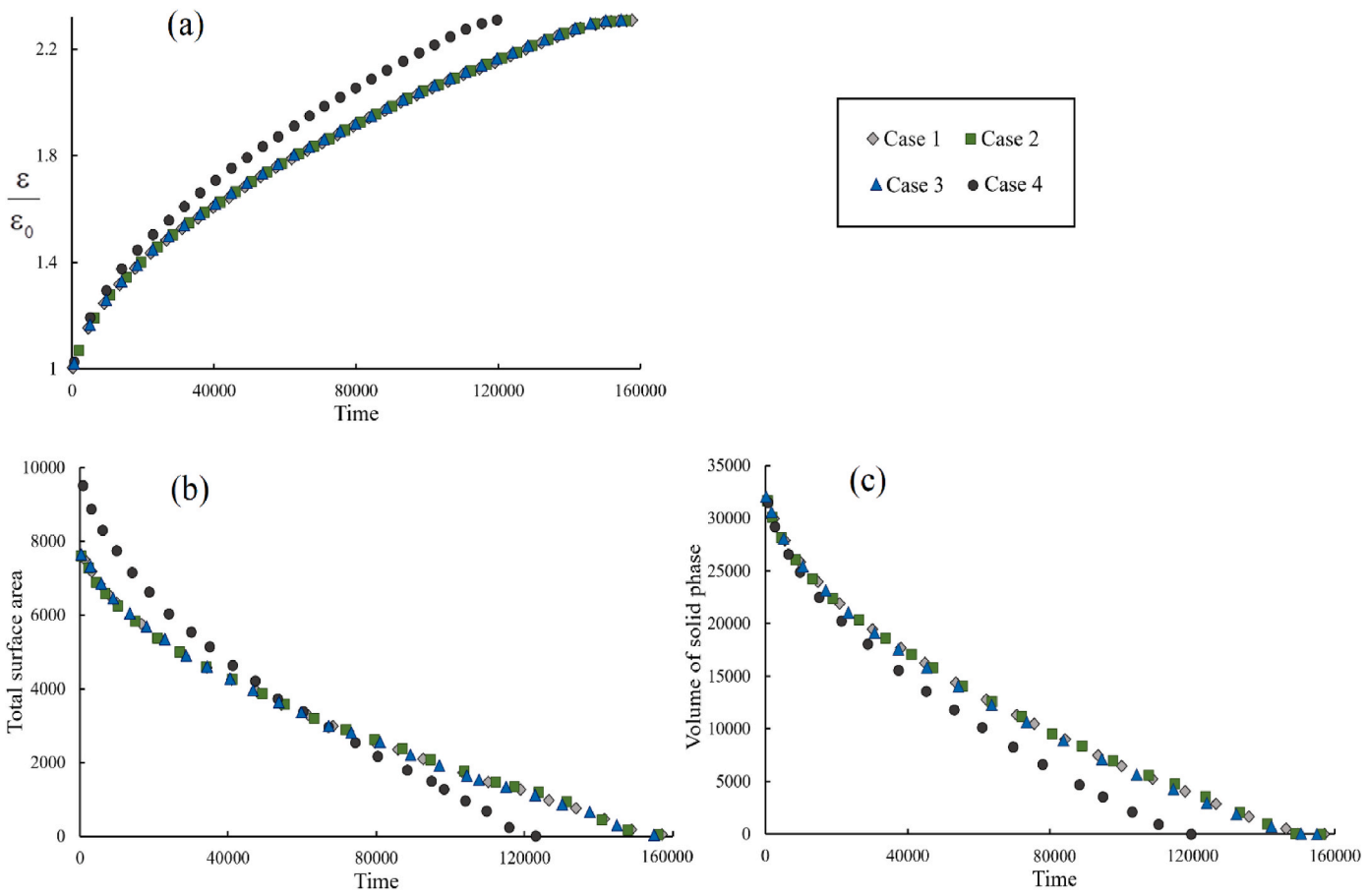


**Fig. 17.** Evolution of (a) the normalized porosity, (b) the surface area, (c), and volume of porous media as a function of time step during face dissolution reactive transport.

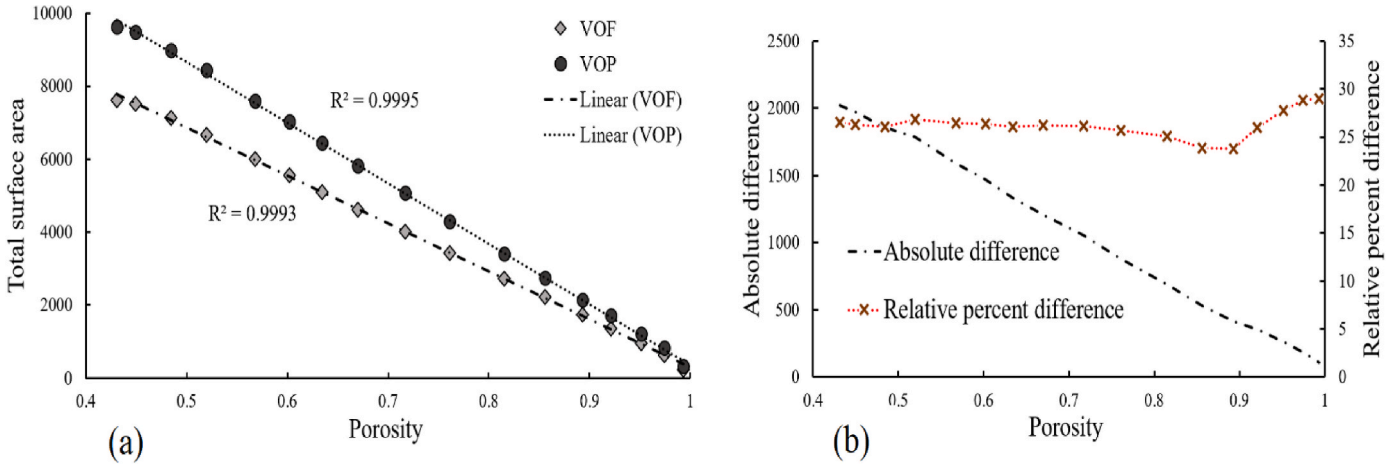


**Fig. 18.** (a) Variation of surface area versus porosity by VOF and VOP method (b) absolute difference and relative percent difference of surface area of VOP relative to VOF method in face dissolution.

Fig. 21 shows the temporal evolution of the normalized porosity (Fig. 21 (a)), the surface area (Fig. 21 (b)) and the solid volume (Fig. 21 (c)) of the porous medium during the dissolution process. All cases except the 4th scenario show similar trends while the faster dissolution of case 4 is obvious. It should be noted that the similarities between the 4 trends at large time steps in Fig. 21 (a) are mainly due to the asymptotic nature of the uniform dissolution and should not be misinterpreted as an equivalence of the methods at this extreme. By using the VOP method the medium dissolves almost 21% faster, at any instant of time in plots of Fig. 21, the calculated porosity using the VOP method would be substantially different from the other three cases. Therefore, the same time steps in these figures refer to different stages of dissolution for the VOP and the VOF method and their comparison should be performed with care.

Variation of the surface area with porosity change is shown in Fig. 22 (a). As the results from the three VOF cases were nearly the same only

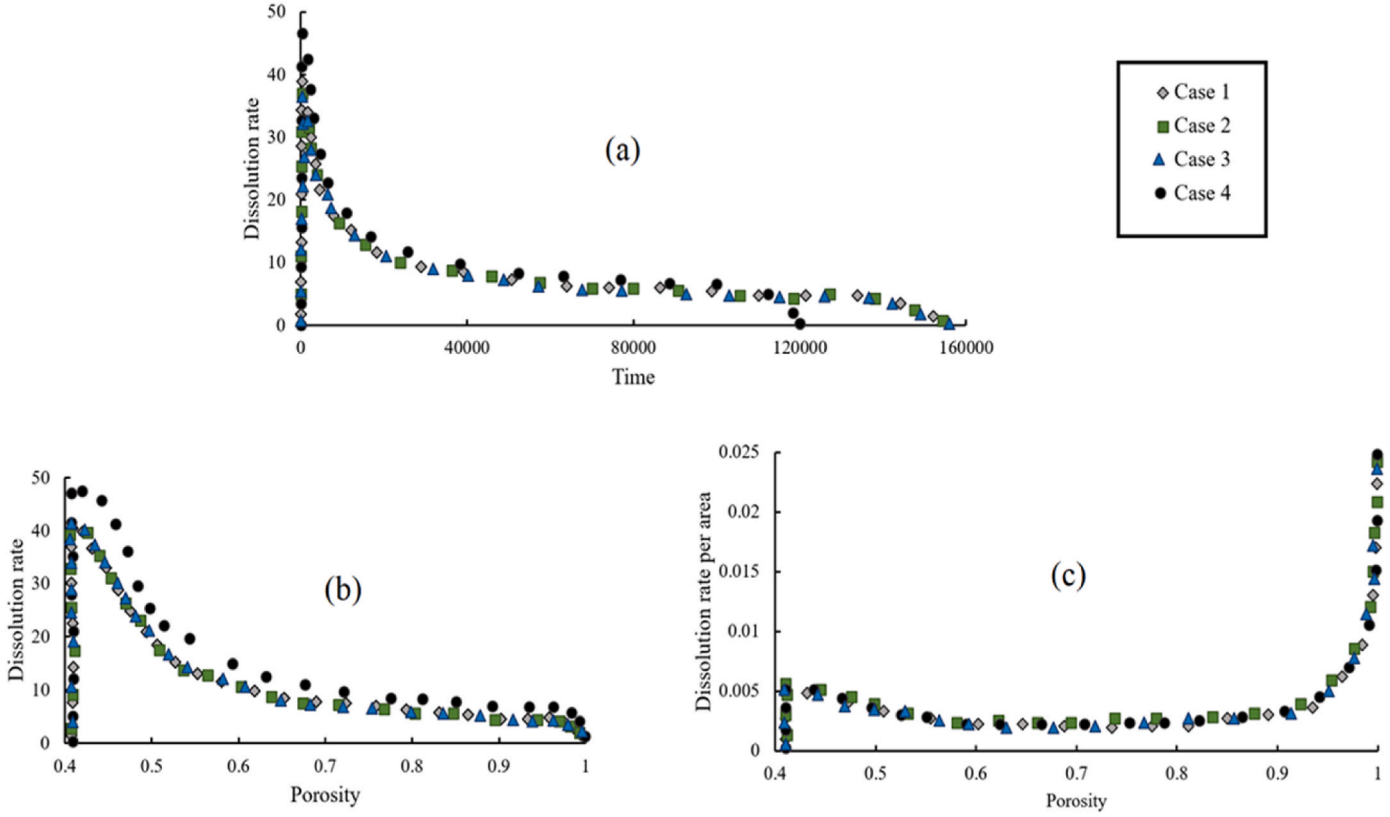


**Fig. 19.** Variation of dissolution rate with time (a) and porosity (b) together with the variation of dissolution rate (normalized by surface area) with porosity (c) in the face dissolution regime.

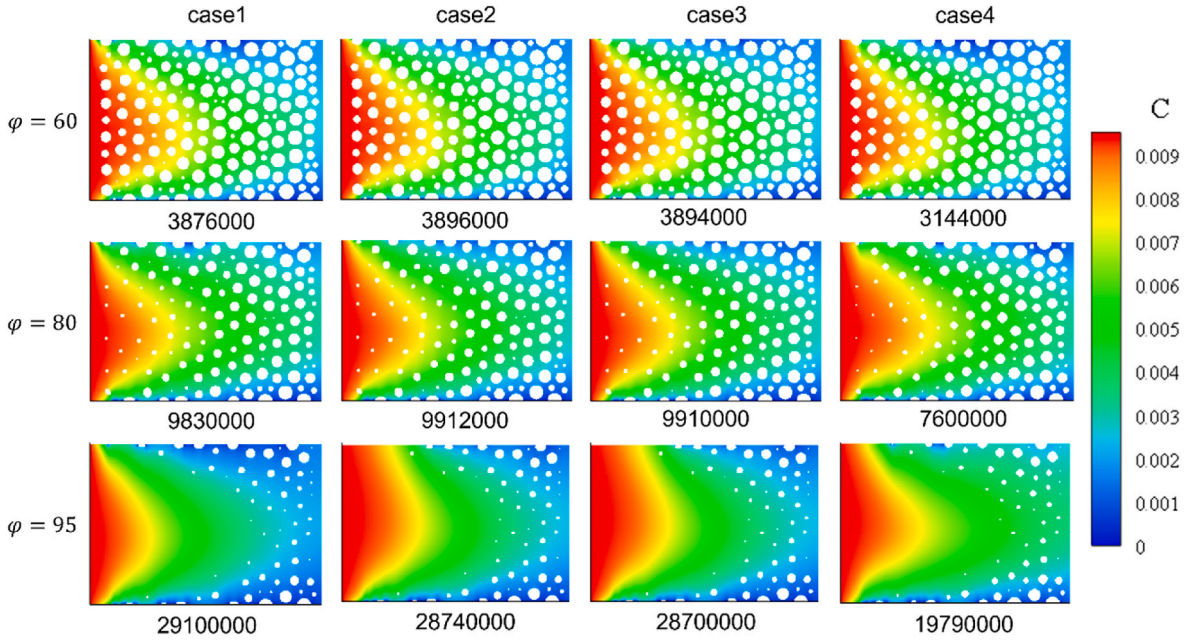


**Fig. 20.** Dissolution patterns and their associated time steps at 60, 80, and 95% porosity values for the four cases at Pe = 6.5 and Da = 0.01.

two trends labeled as VOF and VOP are shown. The calculated surface area of the VOP method is clearly higher than that of the VOF method at the same stage of dissolution (i.e., at the same porosity values) following the trend of a decreasing polynomial of the second degree. Fig. 22 (b) shows the absolute and relative percent difference between the calculated surface area by the VOF and the VOP methods. Although the absolute difference between the two methods reduces by increasing porosity their relative difference increases almost linearly with an average value of 31%. This indicates that under this dissolution regime, the difference between the VOP and the VOF methods would be more pronounced compared to the surface dissolution regime. We should note that the relative difference for a uniform dissolution regime has a strictly

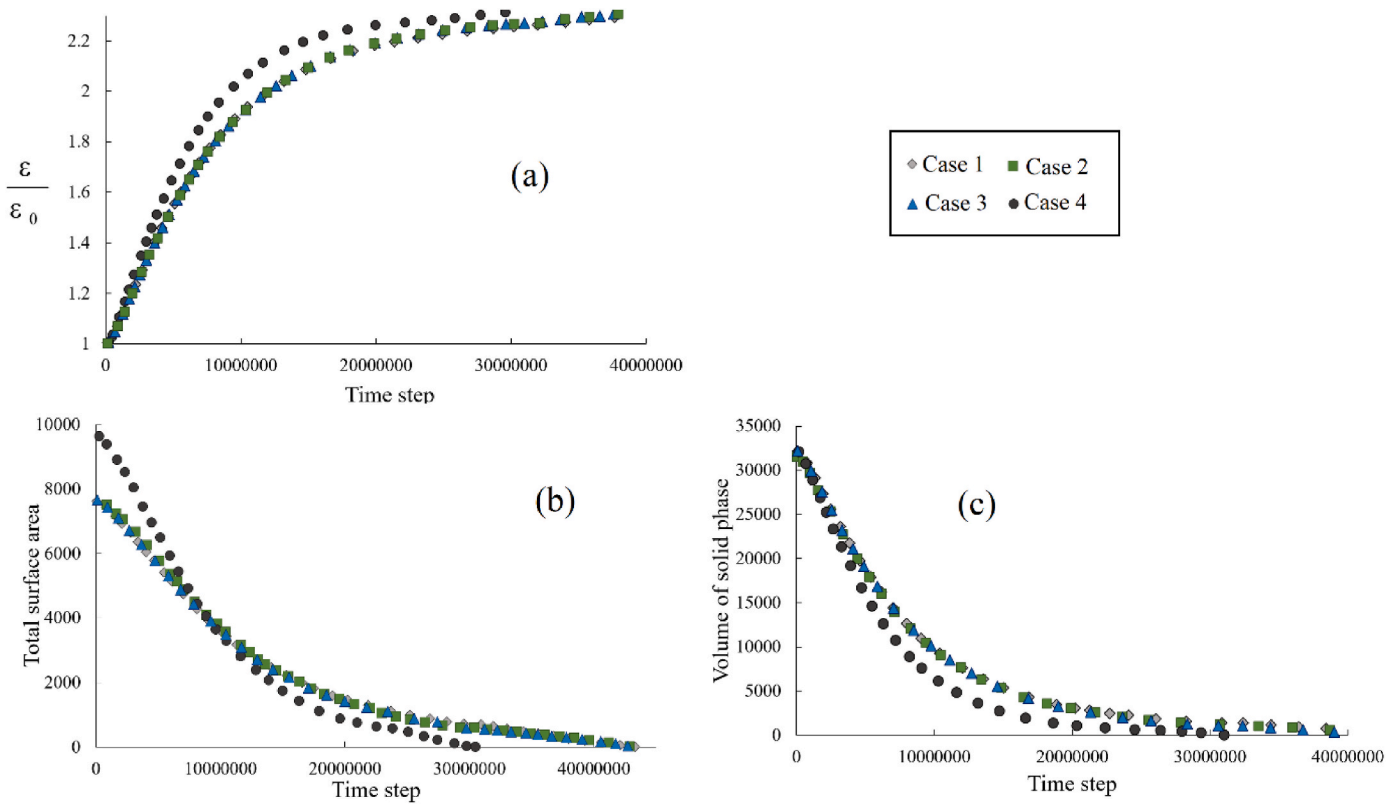


**Fig. 21.** Evolution of (a) the normalized porosity, (b) the surface area, and (c) the solid volume of the porous medium as a function of time step under the uniform dissolution regime.

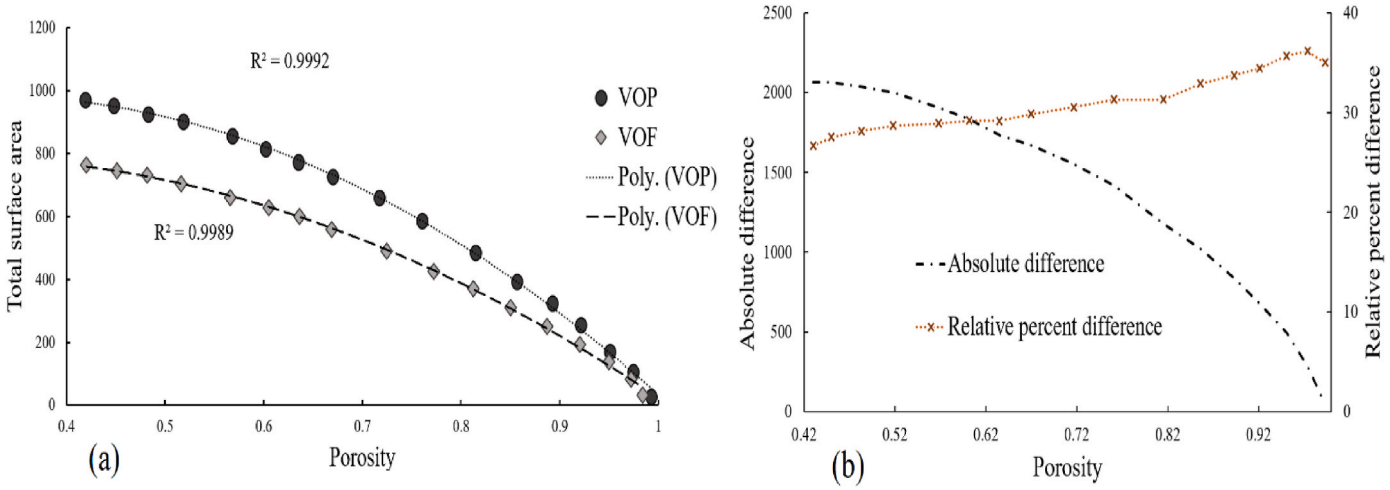


**Fig. 22.** (a) Variation of the surface area with porosity by VOF and VOP methods (b) absolute difference and relative percent difference of surface area of VOP relative to VOF method in uniform dissolution regime.

increasing trend which shows that by the progress of the dissolution the temporal errors of the VOP method increase.

Fig. 23 (a) shows the variation of dissolution rate over time. As expected, a larger surface area when using the VOP method led to sharper peaks of dissolution rate and 21% faster dissolution. In addition, Fig. 23 (b) shows the variation of dissolution rate versus porosity which is in agreement with previous results. At similar stages of dissolution (i.e., similar porosities) the VOP method provides higher dissolution rates while no considerable difference between the results of the other cases is observed. The departure among the trends of Fig. 23 (b) is substantially due to surface area effects. Since there is no meaningful difference among the four cases as seen in Fig. 23 (c), which represents the normalized dissolution rates by their associated surface area. This also indicates that despite the dramatic effects of surface tracking on temporal results, the tracking surface area and the choice of hydrodynamic boundary conditions do not impact the shape and pattern of dissolutions.

## 5. Computational time

In this section, we explore the computational time of the algorithms. We should note that various factors including the language of coding,

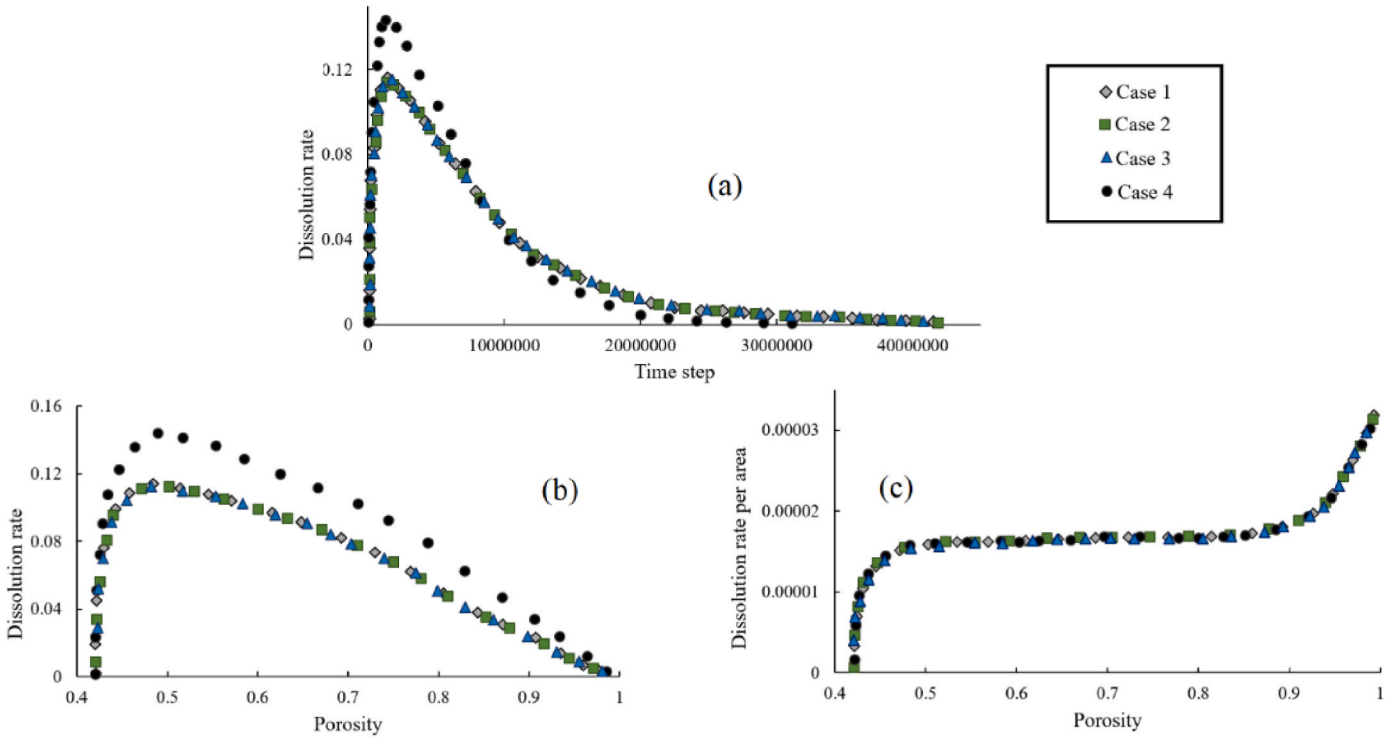


**Fig. 23.** Variation of dissolution rate with time (a) and the porosity (b) together with the variation of dissolution rate, normalized by surface area, with porosity change (c) in a uniform dissolution regime.

depth and method of parallelization, employed hardware, and memory management would also significantly affect the performance of the algorithms. Such an in-depth analysis is beyond the scope of this study and we report the CPU times associated with each algorithm. A computing system equipped with CPU intel i7-4790 k (4.00 GHz), 32.0 GB RAM and Windows 7 ultimate operating system was prepared and intel FORTRAN was used as the programming language. Dissolution simulations for both single grain and porous medium were tested for $10^6$ iterations and their corresponding times are provided in Table 3. As the VOP method is popular in LBM framework for simulating heterogeneous dissolutions, all computation times were compared with that of the VOP method (i.e., case 4).

For both single grain geometry and complex porous medium geometry, employment of the VOF method with bounce-back boundary conditions has led to about 4–5 percent increase in the computational times. However, the use of the simplified curved boundary or the full curved boundary scheme would almost double or triple the increase, respectively. This finding and the previous results indicate that as long as a very accurate reconstruction of solid curvatures is not required, the most efficient and reliable method of simulating a dissolving medium is to employ the VOF method and use the standard bounce back approach as the hydrodynamic boundary condition.

**Table 3**
Computation time necessary for $10^6$ iterations of a dissolving grain and dissolving porous medium. Values in parenthesis are the increase in time relative to VOP method.

| | Time (minutes) | | | |
|---|---|---|---|---|
| | Case 1 | Case 2 | Case 3 | Case 4 |
| Grain | 119.4 (3.8%) | 130.1 (13.1%) | 123.3 (7.2%) | 115 |
| Porous medium | 284.8 (4.9%) | 316.6 (16.6%) | 298.3 (9.8%) | 271.6 |

## 6. Conclusions

In this study, for implementing curved boundary condition in a heterogeneous dissolution process that involved geometry evolution, a method of combining VOF with curved boundary schemes were presented. Since the combination of the full curved boundary method with VOF would be rather complex, in addition to the original approach, a simplified approximate approach was also introduced, which would require less computational time and offer almost similar accuracy. It was concluded that the employment of curved boundary had no considerable impact on the concentration field and the algorithm of bounce back method was found to be 10% more efficient. Further, the performance of VOP method was compared with that of the VOF surface capturing technique. It was found that VOP method in comparison with VOF overestimated the surface area of the reactions by about 25–35%. This overestimation would lead to artificially 20–30% higher dissolution rates and nearly 20–30% shorter dissolution times, suggesting that from a temporal point of view, the results from VOP method would be invalid. However, from a non-temporal point of view, the patterns of dissolutions of VOF and VOP approaches were found to be essentially similar.

## CRediT author statement

**Elham Kashani:** Investigation, Software, Validation, Formal analysis, Visualization, Writing - Original Draft. **Ali Mohebbi:** Project administration, Conceptualization, Methodology, Writing - Review & Editing, Resources. **Amir Ehsan Feili Monfared:** Conceptualization, Methodology, Writing - Review & Editing. **Amir Raoof:** Conceptualization, Writing - Review & Editing.

## Declaration of competing interest

The authors declare that they have no known competing financial interests or personal relationships that could have appeared to influence the work reported in this paper.

## Appendix

### A. Calculation of q

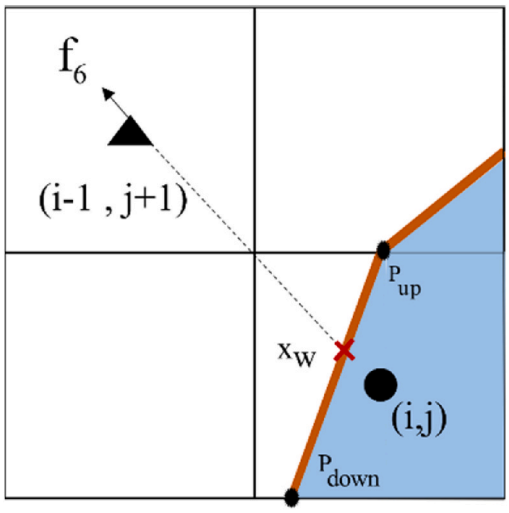


**Fig. A.1.** $P_{up}$, $P_{down}$ and $x_w$ for cell (i,j).

This appendix explains how q is calculated. As an example consider the cell (i,j) in Fig. A1.

$$P_{up}: \begin{cases} x = i - 0.5 + \dfrac{1}{2\tan\theta_{i,j}} - V_{i,j} \\ y = j - 0.5 \end{cases} \quad P_{down}: \begin{cases} x = i - 0.5 - \dfrac{1}{2\tan\theta_{i,j}} - V_{i,j} \\ y = j - 1.5 \end{cases} \tag{A.1}$$

where P represents the intersection points of the interface line with cell boundary and $V_{i,j}$ is the solid volume of the cell. Accordingly, the interface equation would be:

$$y = \tan\theta_{i,j}\left[x - i + 0.5 + \frac{1}{2\tan\theta_{i,j}} + V_{i,j}\right] + j - 1.5 \tag{A.2}$$

One of the challenges of this method is that for the interface nodes with 100% solid fraction, no interface line can be considered. In this case, to work the algorithm properly, a possible approach is to assign a value slightly less than 1 (e.g., 0.9999) to the initial solid volume of such cells.

Once the interface equation is found, the length of intersection of discrete velocity lines with the interface line should be calculated (q). The method of calculating q and $x_w$ for the geometry of Fig. A.1 is as follows:

$$\begin{cases} y = \tan\theta_{i,j}\left[x - i + 0.5 + \dfrac{1}{2\tan\theta_{i,j}} + V_{i,j}\right] + j - 1.5, \text{interface at cell}(i,j) \\ y = -\tan 45(x - i + 1) + j + 1, \text{line parallel with} f_6 \text{ and passing center of cell } (i-1, j+1) \end{cases} \tag{A.3}$$

Intersecting these two lines gives

$$\begin{aligned} x_w &= -\frac{\tan\theta_{i,j}\left(-i + 0.5 + \dfrac{1}{2\tan\theta_{i,j}} + V_{i,j}\right) - 2.5 + \tan 45(1 - i)}{\tan 45 + \tan\theta_{i,j}} \\ y_w &= -\tan 45\left[-\frac{\tan\theta_{i,j}\left(-i + 0.5 + \dfrac{1}{2\tan\theta_{i,j}} + V_{i,j}\right) - 2.5 + \tan 45(1 - i)}{\tan 45 + \tan\theta_{i,j}} - i + 1\right] + j + 1 \end{aligned} \tag{A.4}$$

Finally, the length of the line segment connecting the center of the cell (i-1,j+1) with $x_w$ (i.e., length of $q_6$ (i-1,j+1)) can be calculated and therefore q (Eq. (18)) is calculated as follows:

$$q = \frac{\sqrt{(x_w - (i-1))^2 + (y_w - (j+1))^2}}{\sqrt{2}} \tag{A.5}$$

*B. Pixelizing geometry*

This appendix explains the effect of pixelizing on the surface area. Some sample geometries are illustrated in Fig. B.1. As shown in this figure, generally the curves not parallel to the Cartesian meshes are pixelized into shapes with surface areas higher than their true physical values. For example, in Fig. B.1 (a) and (b), while the true values for the length of the hypotenuse of the triangle and the arc of the quarter circle are 6.71 and 6.28, respectively, the VOP algorithm would allocate 10 and 7 to their area, respectively. This indicates that the percent error of pixelizing may even reach values of around 54%. Even pixelizing straight line segments parallel to the horizontal or vertical Cartesian meshes are not guaranteed to be free of inaccuracies. For example, as shown in Fig. B.1 (c), while both the upper and the lower lines have equal lengths, the lower one is mapped to a greater number of pixels due to its partial length share with neighboring cells. Hence, the only case in that VOP does not overestimate the surface area, would be a straight line parallel to horizontal or vertical Cartesian meshes with no imperfect occupation of the cells.

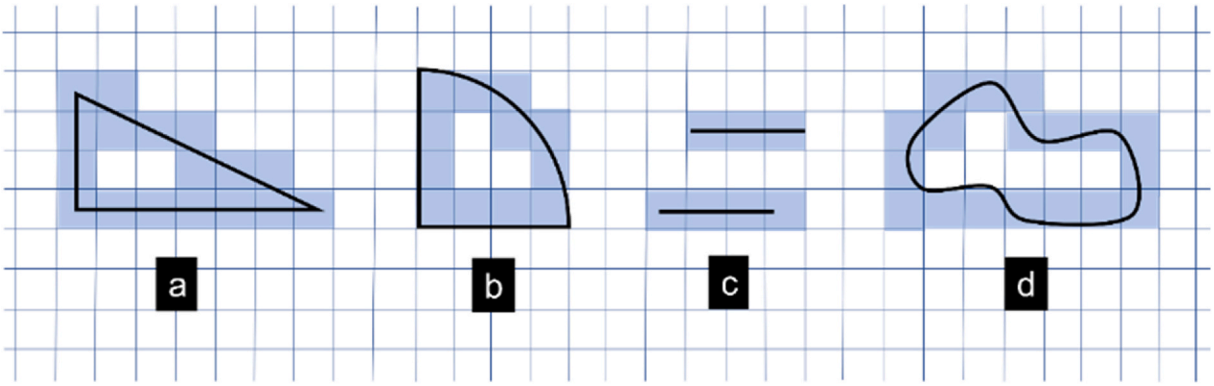


**Fig. B.1.** Four geometries (a, b, c, and d) with a different surface area (black lines) and their pixelized representation (shaded cells).

The presented argument further leads to the inference that for regular shapes with straight boundaries, the dissolution trends of both methods should be closer to each other. For validation of this inference, a second case similar to that of Fig. 7 was also simulated with the same parameters as Table 1. But this time the circular grain at the center of the channel was replaced by a square of side length 0.0002 m. The results of this case are shown in Fig. B.2. As shown, the trend lines are closer in comparison to those of Fig. 11 (a), confirming the deduction.

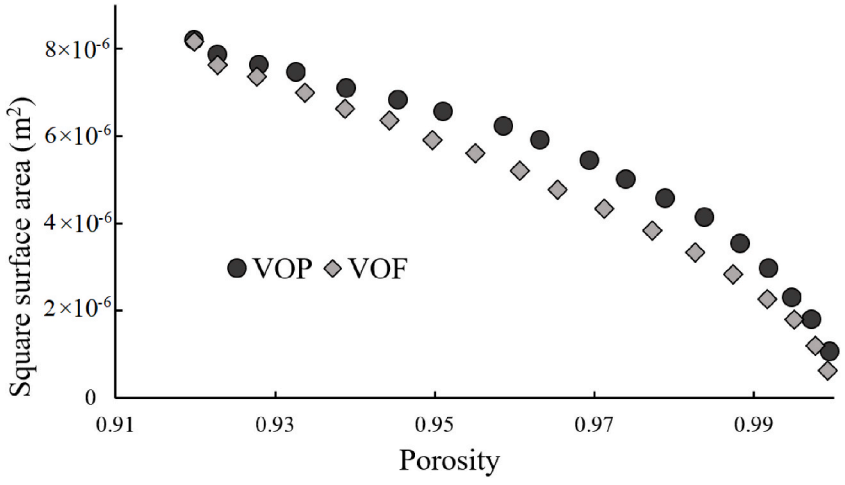


**Fig. B.2.** Variation of the surface area of a square-shaped grain with porosity.

It should be noted that the same presented arguments cannot be generally applied to the grain's total volume. In fact, for volume, both VOP and VOF methods allocate the same values to the initial volume of the pixels and therefore the algorithms start from the same initial conditions. In this case, the initial volume of the interface pixels can be either calculated algebraically with no approximation included (mainly applicable for regular shapes) or should be approximated by assigning 1 to the initial volume of the interface pixels (the common approach for irregular arbitrary shapes like that of Fig. B2 (d)).

## References


T, W.F.N., P, W., 1976. SLIC (simple line interface calculation). In: van Dooren, A.I., Zandbergen, P.J. (Eds.), Lect. Notes Phys, vol. 59, pp. 330–340.

Bouzidi, M., Firdaouss, M., Lallemand, P., 2001. Momentum transfer of a Boltzmann-lattice fluid with boundaries. Phys. Fluids 13, 3452–3459. https://doi.org/10.1063/1.1399290.

Chang, C., Liu, C.H., Lin, C.A., 2009. Boundary conditions for lattice Boltzmann simulations with complex geometry flows. Comput. Math. Appl. 58, 940–949. https://doi.org/10.1016/j.camwa.2009.02.016.

Chen, L., Kang, Q., Robinson, B.A., He, Y.L., Tao, W.Q., 2013. Pore-scale modeling of multiphase reactive transport with phase transitions and dissolution-precipitation processes in closed systems. Phys. Rev. E 87, 1–16. https://doi.org/10.1103/PhysRevE.87.043306.

Chen, L., Kang, Q., Carey, B., Tao, W.Q., 2014. Pore-scale study of diffusion-reaction processes involving dissolution and precipitation using the lattice Boltzmann method. Int. J. Heat Mass Tran. 75, 483–496. https://doi.org/10.1016/j.ijheatmasstransfer.2014.03.074.

Chen, L., Kang, Q., Tang, Q., Robinson, B.A., He, Y.L., Tao, W.Q., 2015. Pore-scale simulation of multicomponent multiphase reactive transport with dissolution and precipitation. Int. J. Heat Mass Tran. 85, 935–949. https://doi.org/10.1016/j.ijheatmasstransfer.2015.02.035.

Chun, B., Ladd, A.J.C., 2007. Interpolated boundary condition for lattice Boltzmann simulations of flows in narrow gaps. Phys. Rev. E 75, 1–12. https://doi.org/10.1103/PhysRevE.75.066705.

Cui, S., Hong, N., Shi, B., Chai, Z., 2016. Discrete effect on the halfway bounce-back boundary condition of multiple-relaxation-time lattice Boltzmann model for convection-diffusion equations. Phys. Rev. E 43311, 1–13. https://doi.org/10.1103/PhysRevE.93.043311.

Dugast, F., Favennec, Y., Josset, C., 2020. Reactive fluid flow topology optimization with the multi-relaxation time lattice Boltzmann method and a level-set function. J. Comput. Phys. 409, 109252 https://doi.org/10.1016/j.jcp.2020.109252.

Duquerroix, J.P., Defives, D., Labrid, J., 1990. Dissolution processes associated with the injection of alkaline solutions into clayey sandstone formations. J. Pet. Sci. Eng. 4, 43–56. https://doi.org/10.1016/0920-4105(90)90045-5.

d'Humières, D., Ginzburg, I., 2009. Viscosity independent numerical errors for Lattice Boltzmann models: from recurrence equations to "magic" collision numbers. Comput. Math. Appl. 58, 823–840. https://doi.org/10.1016/j.camwa.2009.02.008.

Fogler, H.S., Hoefner, M.L., 1988. Pore evolution and channel formation during flow and reaction in porous media. AIChE J. 34, 45–54.

Fredd, C.N., Fogler, H.S., 1998. Influence of transport and reaction in porous media. AIChE J. 44, 1933–1949. https://doi.org/10.1002/aic.690440902.

Ginzburg, I., 2005a. Equilibrium-type and link-type lattice Boltzmann models for generic advection and anisotropic-dispersion equation. Adv. Water Resour. 28, 1171–1195. https://doi.org/10.1016/j.advwatres.2005.03.004.

Ginzburg, I., 2005b. Generic boundary conditions for lattice Boltzmann models and their application to advection and anisotropic dispersion equations. Adv. Water Resour. 28, 1196–1216. https://doi.org/10.1016/j.advwatres.2005.03.009.

Ginzburg, I., D'Humières, D., 2003. Multireflection boundary conditions for lattice Boltzmann models. Phys. Rev. E 68, 1–30. https://doi.org/10.1103/PhysRevE.68.066614.

Ginzburg, I., d'Humières, D., 2015. Multi-reflection boundary conditions for lattice Boltzmann models. Phys. Rev. E 68. https://doi.org/10.1103/PhysRevE.68.066614.

Griebler, C., Brielmann, H., Haberer, C.M., Kaschuba, S., Kellermann, C., Stumpp, C., Hegler, F., Kuntz, D., Walker-Hertkorn, S., Lueders, T., 2016. Potential impacts of geothermal energy use and storage of heat on groundwater quality, biodiversity, and ecosystem processes. Environ. Earth Sci. 75, 1–18. https://doi.org/10.1007/s12665-016-6207-z.

Guo, Z., Zhao, T.S., 2002. Lattice Boltzmann model for incompressible flows through porous media. Phys. Rev. E 66, 1–9. https://doi.org/10.1103/PhysRevE.66.036304.

Guo, Z., Zheng, C., Shi, B., 2002. An extrapolation method for boundary conditions in lattice Boltzmann method. Phys. Fluids 14, 2007–2010. https://doi.org/10.1063/1.1471914.

Han, J., Han, S., Kang, D.H., Kim, Y., Lee, J., Lee, Y., 2020. Application of digital rock physics using X-ray CT for study on alteration of macropore properties by CO2 EOR in a carbonate oil reservoir. J. Pet. Sci. Eng. 189, 107009 https://doi.org/10.1016/j.petrol.2020.107009.

He, X., Zou, Q., Luo, L.S., Dembo, M., 1997. Analytic solutions of simple flows and analysis of nonslip boundary conditions for the lattice Boltzmann BGK model. J. Stat. Phys. 87, 115–136. https://doi.org/10.1007/BF02181482.

He, X., Chen, S., Doolen, G.D., 1998. A novel thermal model for the lattice Boltzmann method in incompressible limit. J. Comput. Phys. 146, 282–300.

Hoop, S. de, Jones, E., Voskov, D., 2021. Accurate geothermal and chemical dissolution simulation using adaptive mesh refinement on generic unstructured grids. Adv. Water Resour. 154, 1–17. https://doi.org/10.1016/j.advwatres.2021.103977.

Izam, M., Fukui, T., Morinishi, K., 2011. Application of regularized lattice Boltzmann method for incompressible flow simulation at high Reynolds number and flow with curved boundary. J. Fluid Sci. Technol. 6, 812–822. https://doi.org/10.1299/jfst.6.812.

Jiang, M., Xu, Z.G., Zhou, Z.P., 2021. Pore-scale investigation on reactive flow in porous media considering dissolution and precipitation by LBM. J. Pet. Sci. Eng. 204 https://doi.org/10.1016/j.petrol.2021.108712.

Ju, L., Zhang, C., Guo, Z., 2020. Local reactive boundary scheme for irregular geometries in lattice Boltzmann method. Int. J. Heat Mass Tran. 150, 119314 https://doi.org/10.1016/j.ijheatmasstransfer.2020.119314.

Kang, Q., Zhang, D., Chen, S., 2003. Simulation of dissolution and precipitation in porous media. J. Geophys. Res. Solid Earth 108, 1–10. https://doi.org/10.1029/2003jb002504.

Kang, Q., Lichtner, P.C., Zhang, D., 2007. An improved lattice Boltzmann model for multicomponent reactive transport in porous media at the pore scale. Water Resour. Res. 43, 1–12. https://doi.org/10.1029/2006WR005551.

Kang, Q., Chen, L., Valocchi, A.J., Viswanathan, H.S., 2014. Pore-scale study of dissolution-induced changes in permeability and porosity of porous media. J. Hydrol. 517, 1049–1055. https://doi.org/10.1016/j.jhydrol.2014.06.045.

Kao, P.H., Yang, R.J., 2008. An investigation into curved and moving boundary treatments in the lattice Boltzmann method. J. Comput. Phys. 227, 5671–5690. https://doi.org/10.1016/j.jcp.2008.02.002.

Kothe, D.B., 1991. RIPPLE: a computer program for incompressible flows with free surfaces. Comput. Sci. 1 https://doi.org/10.13140/RG.2.1.1397.5200.

Lallemand, P., Luo, L., 2000. Theory of the lattice Boltzmann method: dispersion, dissipation, isotropy, Galilean invariance, and stability. Phys. Rev. E 61, 628–632. https://doi.org/10.1103/PhysRevE.61.6546.

Li, C., Maa, J.P.Y., 2017. Multi-relaxation-time lattice Boltzmann simulations of lid driven flows using graphics processing unit. Appl. Math. Mech. (English Ed. 38, 707–722. https://doi.org/10.1007/s10483-017-2194-9.

Li, X., Huang, H., Meakin, P., 2008. Level set simulation of coupled advection-diffusion and pore structure evolution due to mineral precipitation in porous media. Water Resour. Res. 44, 1–17. https://doi.org/10.1029/2007WR006742.

Liu, M., Shabaninejad, M., Mostaghimi, P., 2018. Predictions of permeability, surface area and average dissolution rate during reactive transport in multi-mineral rocks. J. Pet. Sci. Eng. 170, 130–138. https://doi.org/10.1016/j.petrol.2018.06.010.

Ma, X., Mou, J., Lin, H., Jiang, F., Liu, K., Zhao, X., 2017. Lattice Boltzmann simulation of wormhole propagation in carbonate acidizing. J. Energy Resour. Technol. 139, 1–19. https://doi.org/10.1115/1.4035909.

Martinez, J.M., Chesneau, X., Zeghmati, B., 2006. A new curvature technique calculation for surface tension contribution in PLIC-VOF method. Comput. Mech. 37, 182–193. https://doi.org/10.1007/s00466-005-0689-y.

Mei, R., Yu, D., Shyy, W., Luo, L.S., 2002. Force evaluation in the lattice Boltzmann method involving curved geometry. Phys. Rev. E 65, 14. https://doi.org/10.1103/PhysRevE.65.041203.

Menke, H.P., Bijeljic, B., Andrew, M.G., Blunt, M.J., 2015. Dynamic three-dimensional pore-scale imaging of reaction in a carbonate at reservoir conditions. Environ. Sci. Technol. 49, 4407–4414. https://doi.org/10.1021/es505789f.

Molins, S., Soulaine, C., Prasianakis, N.I., Abbasi, A., Poncet, P., Ladd, A.J.C.C., Starchenko, V., Roman, S., Trebotich, D., Tchelepi, H.A., Steefel, C.I., Secondary, C. A., Author, C., Molins, S., Soulaine, C., Prasianakis, N.I., Abbasi, A., Poncet, P., Ladd, A.J.C.C., Starchenko, V., Roman, S., Trebotich, D., Tchelepi, H.A., Steefel, C.I., Ridge, O., 2020. Simulation of mineral dissolution at the pore scale with evolving fluid-solid interfaces: review of approaches and benchmark problem set. Comput. Geosci. 25, 1285–1318. https://doi.org/10.1007/s10596-019-09903-x.

Mostaghimi, P., Liu, M., Arns, C.H., 2016. Numerical simulation of reactive transport on micro-CT images. Math. Geosci. 48, 963–983. https://doi.org/10.1007/s11004-016-9640-3.

Osher, S., Sethian, J.A., 1988. Fronts propagating with curvature-dependent speed: algorithms based on Hamilton-Jacobi formulations. J. Comput. Phys. 79, 12–49. https://doi.org/10.1016/0021-9991(88)90002-2.

Pan, C., Luo, L., Miller, C.T., 2006. An evaluation of lattice Boltzmann schemes for porous medium flow simulation. Comput. Fluids 35, 898–909. https://doi.org/10.1016/j.compfluid.2005.03.008.

Pilliod, J.E., Puckett, E.G., 2004. Second-order accurate volume-of-fluid algorithms for tracking material interfaces. J. Comput. Phys. 199, 465–502. https://doi.org/10.1016/j.jcp.2003.12.023.

Prasianakis, N.I., Curti, E., Kosakowski, G., Poonoosamy, J., Churakov, S.V., 2017. Deciphering pore-level precipitation mechanisms. Sci. Rep. 7, 1–9. https://doi.org/10.1038/s41598-017-14142-0.

Přikryl, J., Jha, D., Stefánsson, A., Stipp, S., 2017. Mineral dissolution in porous media: an experimental and modeling study on kinetics, porosity and surface area evolution. Appl. Geochem. 87, 57–70. https://doi.org/10.1016/j.apgeochem.2017.05.004.

Quintard, M., Whitaker, S., 1994. Convection, dispersion, and interfacial transport of contaminants: homogeneous porous media. Adv. Water Resour. 17, 221–239. https://doi.org/10.1016/0309-1708(94)90002-7.

Rudman, M., 1997. Volume-tracking methods for interfacial flow calculations. Int. J. Numer. Methods Fluid. 24, 671–691. https://doi.org/10.1002/(SICI)1097-0363(19970415)24:7<671::AID-FLD508>3.0.CO;2-9.

Scardovelli, R., Zaleski, S., 1999. Direct numerical simulation of free-surface and interfacial flow. Annu. Rev. Fluid Mech. 31, 567–603. https://doi.org/10.1146/annurev.fluid.31.1.567.

Shin, Y.H., Hong, C.P., 2002. Modeling of dendritic growth with convection using a modified. ISIJ Int. 42, 359–367.

Taahodi, M., Mohebbi, A., Feili Monfared, A.E., 2021. Lattice Boltzmann study of porosity-permeability variation in different regimes of non-isothermal dissolution in porous media. J. Pet. Sci. Eng. 202.

Tan, L., Zabaras, N., 2006. A level set simulation of dendritic solidification with combined features of front-tracking and fixed-domain methods. J. Comput. Phys. 211, 36–63. https://doi.org/10.1016/j.jcp.2005.05.013.

Tan, L., Zabaras, N., 2007. A level set simulation of dendritic solidification of multi-component alloys. J. Comput. Phys. 221, 9–40. https://doi.org/10.1016/j.jcp.2006.06.003.

Tong, X., Beckermann, C., Karma, A., Li, Q., 2001. Phase-field simulations of dendritic crystal growth in a forced flow. Phys. Rev. E 63, 1–16. https://doi.org/10.1103/PhysRevE.63.061601.

Wang, M., Zhu, W., 2018. Pore-scale study of heterogeneous chemical reaction for ablation of carbon fibers using the lattice Boltzmann method. Int. J. Heat Mass Tran. 126, 1222–1239. https://doi.org/10.1016/j.ijheatmasstransfer.2018.05.133.

Xu, L., Rao, P., Schaefer, L., 2016. A novel scheme for curved moving boundaries in the lattice Boltzmann method. Int. J. Mod. Phys. C 27, 1–22. https://doi.org/10.1142/S0129183116501448.

Yin, X., Zhang, J., 2012. An improved bounce-back scheme for complex boundary conditions in lattice Boltzmann method. J. Comput. Phys. 231, 4295–4303. https://doi.org/10.1016/j.jcp.2012.02.014.

Yoon, H., Kang, Q., Valocchi, A.J., 2015. Lattice Boltzmann-based approaches for pore-scale reactive transport. Rev. Mineral. Geochem. 80, 393–431.

You, J., Lee, K.J., 2021. A pore–scale investigation of surface roughness on the evolution of natural fractures during acid dissolution using DBS method. J. Pet. Sci. Eng. 204, 108728 https://doi.org/10.1016/j.petrol.2021.108728.

Youngs, D.L., 1984. An Interface Tracking Method for a 3D Eulerian Hydrodynamics Code. Awre Technical.

Yu, D., Mei, R., Luo, L.S., Shyy, W., 2003. Viscous flow computations with the method of lattice Boltzmann equation. Prog. Aero. Sci. 39, 329–367. https://doi.org/10.1016/S0376-0421(03)00003-4.

Zhang, T., Shi, B., Guo, Z., Chai, Z., Lu, J., 2012. General bounce-back scheme for concentration boundary condition in the lattice-Boltzmann method. Phys. Rev. E 85, 1–14. https://doi.org/10.1103/PhysRevE.85.016701.

Zhang, Y., Jiang, F., Tsuji, T., 2022. Influence of pore space heterogeneity on mineral dissolution and permeability evolution investigated using lattice Boltzmann method. Chem. Eng. Sci. 247, 117048 https://doi.org/10.1016/j.ces.2021.117048.

Zhou, X., Xu, Z., Xia, Y., Li, B., Qin, J., 2020. Pore-scale investigation on reactive flow in porous media with immiscible phase using lattice Boltzmann method. J. Pet. Sci. Eng. 191, 107224 https://doi.org/10.1016/j.petrol.2020.107224.

Zou, Q., He, X., 1997. On pressure and velocity boundary conditions for the lattice Boltzmann BGK model. Phys. Fluids 9, 1591–1598. https://doi.org/10.1063/1.869307.

# Update

**Journal of Petroleum Science and Engineering**

**Volume 218, Issue , November 2022, Page**

**DOI: https://doi.org/10.1016/j.petrol.2022.111008**

Journal of Petroleum Science and Engineering 218 (2022) 111008

Contents lists available at ScienceDirect

Journal of Petroleum Science and Engineering

journal homepage: www.elsevier.com/locate/petrol

# Corrigendum to "Lattice Boltzmann study of dissolution in porous media: Comparison of VOP with VOF-curved boundary coupling" [J. Petrol. Sci. Eng., 216 (2022) 110754]

Elham Kashani [a], Ali Mohebbi [a], Amir Ehsan Feili Monfared [b,*], Amir Raoof [c]

[a] Department of Chemical Engineering, Faculty of Engineering, Shahid Bahonar University of Kerman, Kerman, Iran
[b] Department of Chemical Engineering, Graduate University of Advanced Technology, Kerman, Iran
[c] Environmental Hydrogeology, Department of Earth Sciences, Utrecht University, Utrecht, the Netherlands

The authors regret that there is a mistake in equation (31). The correct form of equation (31) in section 4.2 is $R = -\frac{1}{V_m}\frac{dV}{dt}$

Also, the supporting sentence above equation (31) should be corrected as:

"For this purpose, the volume changes of the grain at each time step were divided by its molar volume".

The authors would like to apologise for any inconvenience caused.

DOI of original article: https://doi.org/10.1016/j.petrol.2022.110754.
* Corresponding author.
*E-mail addresses:* amohebbi@uk.ac.ir, amohebbi2002@yahoo.com (A. Mohebbi), e.monfared@kgut.ac.ir (A.E. Feili Monfared), a.raoof@uu.nl (A. Raoof).

https://doi.org/10.1016/j.petrol.2022.111008

Available online 1 October 2022
0920-4105/© 2022 Elsevier B.V. All rights reserved.